Simulation studies and design of AlInGaN-ZnSiGeN_2 quantum wells for high-efficiency ultraviolet light emitters

Thesis

Presented in Partial Fulfillment of the Requirements for the Degree Master of Science in the Graduate School of The Ohio State University

By

Chenxi Hu

Graduate Program in Electrical and Computer Engineering

The Ohio State University

2020

Thesis Committee

Professor Hongping Zhao, Advisor

Professor Shamsul Arafin

Abstract

Ultraviolet (UV) light emitting diodes (LEDs) have been attracting research interest as an environment-friendly, compact, spectra-tunable, controllable and energy efficient alternative to conventional UV sources for application in a wide range of fields including biochemical sensing, covert-communication, epoxy curing, water treatment and purification. Different quantum well (QW) structures based on AlGaN, which covers the bandgap range from 196 nm to 365 nm, have been investigated for UV-LED applications. Recently, high-Al content AlInN alloy based QWs are also being considered for UV-LED application. However, the external quantum efficiency of UV-LEDs has generally been low due to the large polarization in wurtzite nitride materials as well as poor light extraction efficiency.

Zn-IV-N_2 compounds, namely, $ZnSiN_2$, $ZnGeN_2$ and $ZnSnN_2$ are closely related to the group-III nitrides. $ZnGeN_2$ and $ZnSnN_2$ have been predicted to have the large valence band offset with GaN and AlN, which can be exploited to design band engineered AlInGaN/$ZnSiGeN_2$ heterostructure QW for applications in optoelectronics.

In this thesis, we investigate AlN/AlInGaN/$ZnSiGeN_2$/AlInGaN/AlN heterostructure QWs for applications in UV-LEDs with peak emission wavelength (λ_{peak}) close to 270 nm. In this structure, the $ZnSiGeN_2$ works as the hole confinement layer due to the large valence band offset with AlInGaN. Consequently, the electron-hole wavefunction overlap ($\Gamma_{e\text{-}h}$) in the proposed design enhances remarkably as compared to the $\Gamma_{e\text{-}h}$ in conventional AlN/AlGaN/AlN QWs. A 6-band *k.p* method was used to calculate the band alignments as well as the spontaneous emission spectra and the optical gain spectra of the investigated QW structures. For λ_{peak} ~ 255 – 288 nm, the investigated AlInGaN/$ZnSiGeN_2$ QW structure provided ~4.5X enhancement in $\Gamma_{e\text{-}h}$ as compared to the conventional AlGaN QWs. The peak spontaneous emission intensity and spontaneous emission radiative recombination rate increased to almost 10X in the proposed QW structures as compared to the conventional structure. Similar improvement was also found in the peak TE-polarized optical gain. Therefore, the novel AlInGaN/$ZnSiGeN_2$ based heterostructure QW can potentially be used to obtain the high-efficiency UV lasers.

Acknowledgments

To begin with, I would like to thank my advisor, Professor Hongping Zhao, who guided me to complete the thesis, to promptly supervise and understand my progress. Her attitude that she answered doubts and confusion on time enabled me to be deeply inspired and established a rigorous and realistic scientific attitude while I completed my thesis.

At the same time, I also want to show my appreciation to the other fellows of the group for their valuable advice when I worked on my research work. Md Rezaul Karim taught me how to use the simulation code, introduced me to the physical meaning behind it, and helped me understand it deeply. Moreover, Zixuan Feng provided invaluable suggestions in the simulation, and Yuxuan Zhang taught me to use the LPCVD system. His experimental experience inspired me a lot.

Moreover, I sincerely thank my parents and family members for their material and spiritual support. Without their love, I can't finish my project.

Finally, I sincerely thank all the professors who have enriched my professional knowledge and skills during the two years for their hard guidance and teaching to students.

Vita

Sep. 1993 .... Born – Hefei, China

Sep. 2011 – Jun. 2015 .... B.E. Optical Information Science and Technology, Nanjing University of Aeronautics and Astronautics, China

Sep. 2015 – March. 2018 .... M.S. Optical Information Science and Technology, Nanjing University of Aeronautics and Astronautics, China

Aug. 2018 – Present ....Graduate Student, Electrical and Computer Engineering, The Ohio State University

Fields of Study

Major Field: Electrical and Computer Engineering

Table of Contents

List of Tables

List of Figures

Chapter 1. Introduction and Background

1.1 UV-LEDs Background

Semiconductor light emitting diodes (LEDs) are solid-state sources of electromagnetic waves that offer energy efficient, low cost, long-lasting, environment-friendly, intensity-controllable, color-tunable, and compact-sized alternatives to traditional ultraviolet (UV), visible and infrared (IR) sources. Visible LED-based solid-state lighting (SSL) technologies are (i) replacing the incandescent, fluorescent, and high-intensity-discharge (HID) lamps in almost all types of indoor as well as outdoor illumination applications and (ii) finding unprecedented applications in a wide range of fields, for example, in patient care and horticulture [1]. Similarly, IR LEDs are enjoying expanding applications, for example, in infrared communication, remote sensing and serveilance cameras etc. [2]. On the other hand, UV LEDs, which emit electromagnetic waves with the wavelength shorter than the visible light, have been attracting increasing research interest for their potential application in bio-medicine, environmental protection and public health [3].

The UV portion of the electromagnetic spectra covers a wavelength range from 10 nm to 400 nm. This range is commonly divided into several subranges which are referred to as UV-V (10 – 200 nm), UV-C (200 – 280 nm), UV-B (280 – 315 nm) and UV-A (320 – 400

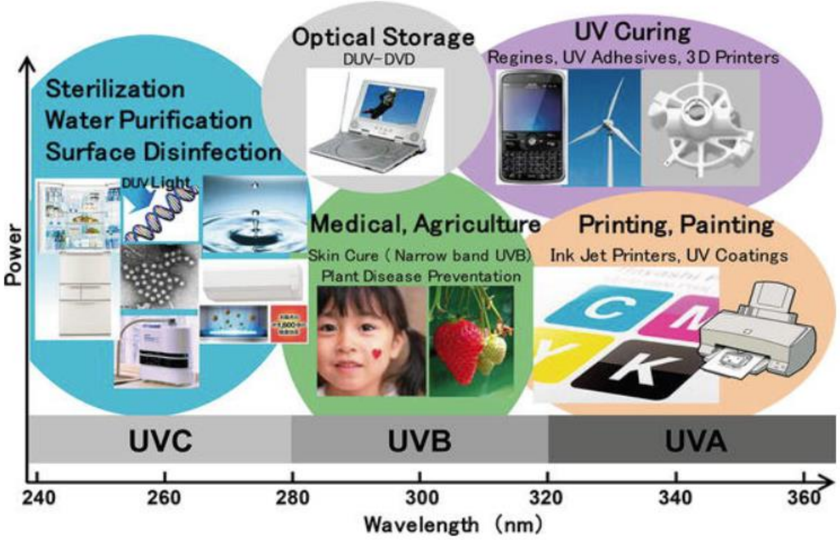

Figure 1.1. Latent utilizations of UV-LEDs [4]

nm). The wavelengths below 320 nm are sometimes referred to as deep UV (DUV). Figure 1.1 [4] shows some applications of UV wavelengths in the range of 240 - 360 nm. Few examples of applications specific UV wavelengths are (i) the use of 360 nm (UV-A) wavelength in pest control, and (ii) use of the 300 – 420 nm wavelengths for vision through windows that block visible lights. Shorter UV wavelengths are widely used in coating curing, pigment curing, photolithography, promoting plant growth, trapping mosquitoes and ultraviolet sterilization. A combined UV and ozone (O_3) based dry surface treatment is gradually replacing the traditional Freon-based wet cleaning processes and becoming an integral step in the manufacturing process of many semiconductor devices, for example, liquid crystal display and other optical products. Moreover, shorter UV-C wavelengths have significant sterilization and disinfection effects. Irradiation of microorganisms such as bacteria and viruses by UV rays disrupts their molecular structure of DNA (deoxyribonucleic acid) or RNA (ribonucleic acid) in the cells of microorganisms, and thus can obstruct its growth [5]. Therefore, UV LEDs can be utilized to develop chemical-free physical disinfection techniques.

1.2 III-Nitrides and II-IV-N_2 Semiconductor Properties

Group-III nitride semiconductors have been extensively investigated for applications in power electronics and optoelectronic, which led to the commercialization of many III-N based technologies including, LEDs and radio frequency (RF) power amplifiers [6]. Binary wurtzite III-N compounds, AlN, GaN and InN have bandgaps of 6.28 eV (~196 nm), 3.4 eV (~365 nm) and 0.64 eV (~1940 nm), respectively. Therefore, the AlInGaN material system covers a wavelength range from UV to visible to IR. Figure 1.2 shows the bandgap vs. lattice constant plot of the III-N material system. Tremendous improvement has been achieved in GaN/InGaN quantum well based blue and violet LEDs. For example, close to 80% external quantum efficiency has been achieved in GaN/InGaN QW based blue LEDs, which has been the work horse in commercial phosphor-converted white LEDs.

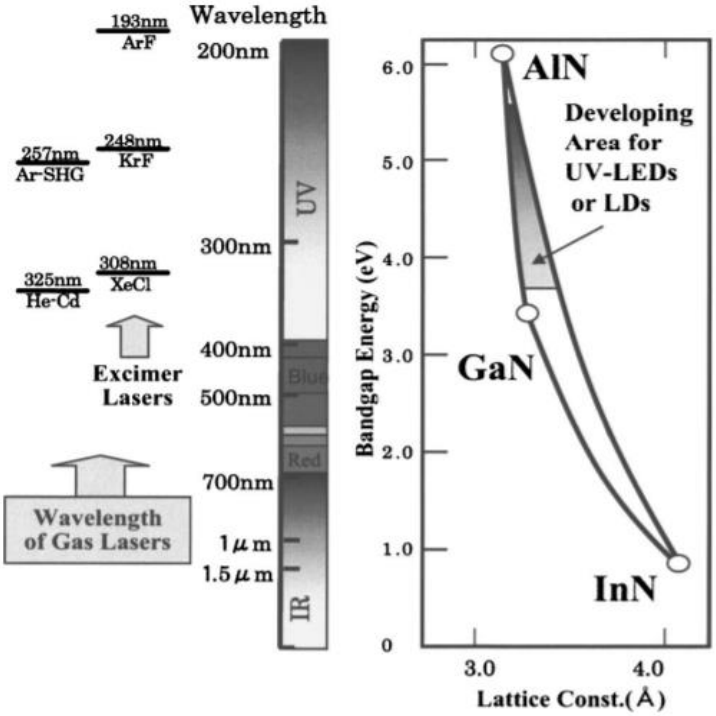

Figure 1.2 Relationship between the direct bandgap and the lattice constant of AlInGaN and the wavelength of gas lasers [7]

On the other hand, AlGaN has been investigated for use as the active layer in UV LEDs. AlGaN based LEDs emitting in 250 nm – 360 nm has been achieved by varying the Al composition in the AlGaN used in the active layer [8-12]. Both single and multi- quantum well structures have been investigated. Compared to the successful blue and violet InGaN LED, the UV-LEDs suffer from low external quantum efficiency (EQE), which has been attributed to (i) low internal quantum efficiency (IQE) and (ii) poor light extraction efficiency. An EQE of 11% in AlGaN based UV emitting 278 nm wavelength was achieved by optimizing the shape and the refractive index [13]. The IQE of AlGaN is sensitive to the threading dislocation density (TDD), which is much lower than that of InGaN. Several approaches have been investigated to suppress the effects of the TDD including the use of multilayer AlN[14]. As can be seen from Figure 1.2, AlInN can also serve as the active layer material in UV LEDs due to its large bandgap, especially when the Al content is high. High-quality n-type AlInN alloys with different In-content have been grown by metalorganic vapor phase epitaxy [15]. Numerical simulations have shown significant improvement in the transverse electrical (TE) mode optical gain and spontaneous emission characteristics of an $Al_{1-x}In_xN$/GaN QW for x~ 0.08 – 0.17[16].

Ternary heterovalent II-IV-N_2 compounds are closely related to the III-Ns and cover a similar bandgap range (0.64 eV – 6.8 eV) as the III-Ns. Among II-IV-N_2s, Zn-IV-N_2 (IV = Si, Ge and Sn) semiconductors have recently been attracting research interest due to their complementary properties to GaN[17]. The bandgaps of $ZnSiN_2$, $ZnGeN_2$ and $ZnSnN_2$ are close to 4.46 eV (experimental result), 3.4 eV and 1.8 eV, respectively. $ZnSiN_2$ is a predicted indirect bandgap material, whereas $ZnGeN_2$ and $ZnSnN_2$ have direct bandgaps. $ZnGeN_2$ is almost lattice-matched with GaN. On the other hand, $ZnSiN_2$ and $ZnSnN_2$ can be lattice-matched with AlInGaN with appropriate alloy compositions. It is also possible to achieve a $ZnSiGeN_2$ compound which is lattice matched with AlInGaN. First-principles-based calculations have predicted more than 1 eV valence band offset of both $ZnGeN_2$ and $ZnSnN_2$ with GaN at the $ZnGeN_2$/GaN and $ZnSnN_2$/GaN heterointerfaces, respectively [18]. In addition, assuming a linear dependence of the valence band position with the alloy composition, it is also possible to achieve similar band alignment between $ZnSiGeN_2$ and $AlInGaN_2$ alloys. Such a large valence band offset between these closely lattice-matched alloys can be exploited to design novel band-engineered device structures for application in optoelectronics. For example, InGaN/$ZnGeN_2$ or InGaN/$ZnSnN_2$ heterostructure QW based LEDs have been predicted to provide remarkable improvement in the efficiency of nitride-based blue, green and amber LEDs [19,20]. In addition, an AlInN/$ZnGeN_2$ based heterostructure has been recently reported for application in high-efficiency DUV LEDs [21].

There have been few reports on the epitaxial growth of $ZnSiN_2$, $ZnGeN_2$ and their quarternary alloy $ZnSiGeN_2$. Single crystalline $ZnSiN_2$ has been achieved on sapphire and SiC substrates by metalorganic chemical vapor deposition (MOCVD) [22-24]. MOCVD growth of $ZnGeN_2$ films has been achieved on c-sapphire [25, 26], r-sapphire [25-27] and a-sapphire [26] substrates. The quarternary $ZnSiGeN_2$ has also been successfully achieved by MOCVD on sapphire and SiC [22,24,28]. In these works, the growth temperatures for the ternary $ZnSiN_2$, $ZnGeN_2$ and the quarternary $ZnSiGeN_2$ alloys all were in the range between 600 – 775 °C. Figure 1.3 shows the variation in the experimentally determined lattice parameter vs. the bandgap of $ZnSiGeN_2$ for different Si compositions [22,28].

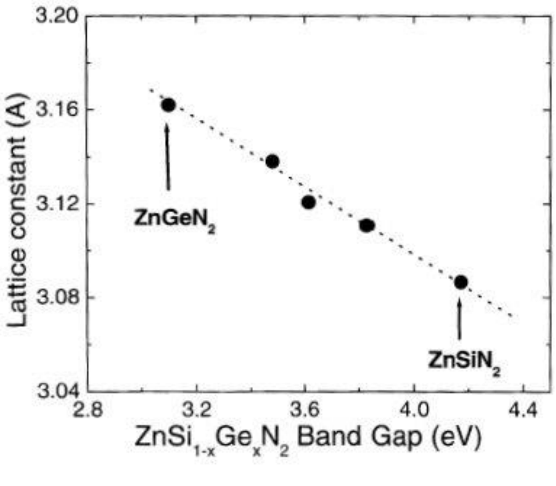

Figure 1.3 The bandgap versus the lattice constant of $ZnSi_{1-x}Ge_xN_2$ [22,28]

The complementary properties between wide bandgap AlInGaN and $ZnSiGeN_2$ alloys provide unique opportunities for designing novel band-engineered light emitters for application in the UV region.

1.3 Research Work and Organization of this Thesis

This thesis reports on a new type AlInGaN/$ZnSiGeN_2$ QW structure with AlN barrier layers for DUV LEDs in the 250-300nm range. A 6-band $\boldsymbol{k} \cdot \boldsymbol{p}$ model was used, taking into account the valence band mixing, the strain, the polarization field and the carrier screening effect [29-31]. Parabolic approximations were made for the electrons. The spontaneous emission spectra and optical gain of the new structure for carrier density ranged from 1×10^{19} to 5×10^{19} cm^{-3} were investigated. The study shows that the insertion of a $ZnSiGeN_2$ layer can provide a notable improvement in the hole carrier confinement, resulting in a ~4 times enhancement of the electron-hole wave function overlap compared with that of the conventional QW. Moreover, a 9-11X improvement in the peak spontaneous emission rate and TE-polarized optical gain was achieved.

In chapter 1, the background of UV-LEDs and the properties of II–IV–N_2 has been discussed.

In chapter 2, the band structure of the AlInGaN/$ZnSiGeN_2$ QW structure was investigated. The wave functions of conventional QW and the novel QW were built.

In chapter 3, the optical gain and spontaneous emission rate of conventional QW and the novel QW were investigated with different $ZnSiGeN_2$ layer thickness and different compositions of each compound.

In chapter 4, the research results and the future works were discussed.

Chapter 2. Design of AlInGaN-ZnSiGeN2 QWs

This chapter focuses on the theoretical and numerical conceptualization of the investigation, including the self-consistent model and the concept of the AlInGaN/ZnSiGeN_2 QW structure. A self-consistent 6-band $\boldsymbol{k \cdot p}$ method is used for calculating the energy band structure in the QW structures. The Hamiltonian for the valence-band structure has been derived recently by this method [29]. By solving Schrodinger's equation for band edge potential using the 6-band $\boldsymbol{k \cdot p}$ method, this novel band structure could be built.

2.1 Conceptual Design

Figure 2.1 (a) shows the bandgap vs. lattice parameter plot of $ZnSiN_2$ and $ZnGeN_2$ along with III-Ns. It is possible to achieve $ZnSiGeN_2$ alloys with close lattice matching with AlGaN and AlInN alloys by tuning the group-IV composition and group-III compositions, respectively. Figure 2.2 (b) shows the band alignment of $ZnSiN_2$ and $ZnGeN_2$ with AlN, InN and GaN. As shown, the conduction and valence band offsets of $ZnGeN_2$ with AlN are $\Delta E_c = -1.2$eV and $\Delta E_v = 1.7$eV, respectively, whereas these values for $ZnSiN_2$ are $\Delta E_c = -0.8$eV and $\Delta E_v = -0.26$eV, respectively [32-34]. For a range of Si composition in $ZnSi_{1-x}Ge_xN_2$ and Al compositions in $Al_{1-x}Ga_xN$ and $Al_{1-x}In_xN$, these alloys will have large valence band offsets, which can potentially be exploited to enhance the electron and hole wavefunction overlap in nitride-based QW LEDs.

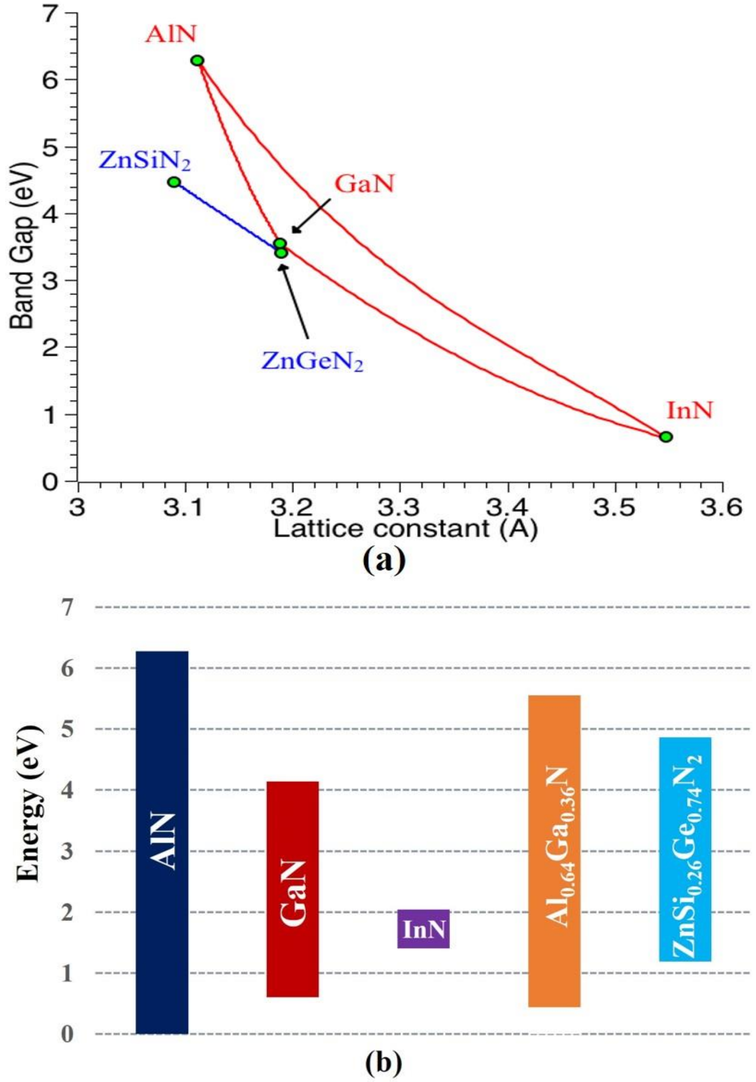

Figure 2.1 (a) The relationship between energy bandgap and lattice constant of III-N and Zn-IV-N_2; (b) Bandgap alignments of AlN, GaN, InN, $Al_{0.64}Ga_{0.36}N$ and $ZnSi_{0.26}Ge_{0.74}N_2$

The polarization induced large internal electric field in III-N quantum wells causes severe band bending, which makes the electron and holes to accumulate in two opposite sides of the QW. Figure 2.2 (a) shows the separation between electron and hole wavefunctions in a conventional AlN/$Al_xGa_{1-x}N$/AlN QW. Figure 2.2 (b) shows the conceptual design of the novel AlN/$Al_{y1}In_{y2}Ga_{1-y1-y2}N$/$ZnSi_wGe_{1-w}N_2$/$Al_{y3}In_{y4}Ga_{1-y3-y4}N$/AlN heterostructure QW structure to be used as the active layer in UV-emitting LEDs. In this structure, the $ZnSiGeN_2$ layer works as the hole confinement layer.

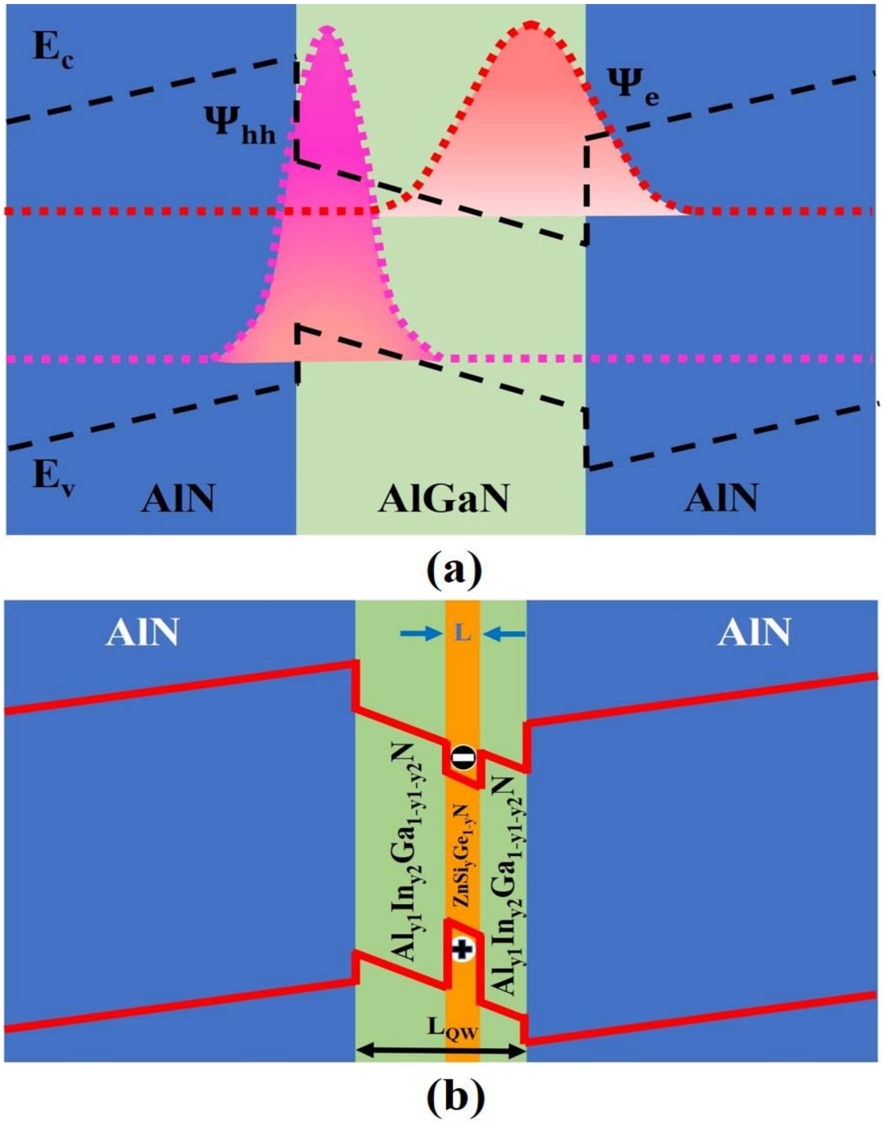

Figure 2.2 (a) Illustration of charge carrier separation in conventional AlGaN QW with AlN barriers; (b) Schematic of the novel AlN/AlInGaN/$ZnSiGeN_2$/AlInGaN/AlN QW

showing the band edge alignment. + and – signs denote low energy regions for holes and electrons, respectively.

2.2 Theoretical and Numerical Methods

The calculation of the electron and hole wave functions is based on a 6-band $\boldsymbol{k}\cdot\boldsymbol{p}$ formalism for the band structure of wurtzite semiconductors [29]. An a 6×6 diagonalized Hamiltonian was used to calculate the hole energy bands. For electrons, the parabolic energy band assumption was made. The model considers the valence band mixing, the strain, the polarization field, and the carrier screening effect.

The conduction bands can be characterized by a parabolic-band model, and the effective-mass Hamiltonian can be written as: [30]

$$H^c(k_t, k_z) = \left(\frac{\hbar^2}{2}\right)\left(\frac{k_t^2}{m_e^t} + \frac{k_z^2}{m_e^z}\right) + E_c^0(z) + P_{c\epsilon}(z) \tag{2.1}$$

where the wave vector $k_t = -i\nabla_t, k_z = -i\,\partial/\partial z$, and m_e^t and m_e^z are respectively the effective electron masses on perpendicular and parallel growth direction.

The conduction-band-edge energy $E_n^c = E_n^c(k_t = 0)$ is determined by solving the effective-mass equation for electrons [30]

$$H^c(k_t = 0, k_z = -i\,\partial/\partial z)\phi_n(z) = E_n^c\phi_n(z) \tag{2.2}$$

with the envelope function normalized as

$$\int dz|\phi_n(z)|^2 = 1 \tag{2.3}$$

For getting the conduction-band structure,

$$E_n^c(k_t) \approx E_n^c(k_t = 0) + \frac{\hbar^2 k_t^2}{2m_{e,w}^t} \tag{2.4}$$

where the $m_{e,w}^{t}$ is the electron effective mass in the well region parallel to the quantum well region. By finding the eigenvalues of the equation (2.5),

$$det\left[H_{ij}^{v}(k) - \delta_{ij}E^{v}(k)\right] = 0 \tag{2.5}$$

the bulk valence-band structure could be built. The electron energy bands are assumed to be parabolic. The Hamiltonian for the valence-band structure has been derived by the $\boldsymbol{k}\cdot\boldsymbol{p}$ method [29]. The hole energy bands can be expressed by using the six-by-six diagonalized $\boldsymbol{k}\cdot\boldsymbol{p}$ Hamiltonian matrix [35]

$$H_{6\times6}^{v}(k) = \begin{bmatrix} H_{3\times3}^{U}(k) & 0 \\ 0 & H_{3\times3}^{L}(k) \end{bmatrix} \tag{2.6}$$

where $H_{3\times3}^{U}(k)$ and $H_{3\times3}^{L}(k)$ are three-by-three matrices defined as

$$H^{U} = \begin{bmatrix} F & K_t & -iH_t \\ K_t & G & \Delta - iH_t \\ iH_t & \Delta + iH_t & \lambda \end{bmatrix} \tag{2.7}$$

$$H^{L} = \begin{bmatrix} F & K_t & iH_t \\ K_t & G & \Delta + iH_t \\ -iH_t & \Delta - iH_t & \lambda \end{bmatrix} \tag{2.8}$$

$$H^{U} = (H^{L})^{*} = (H^{L})^{t} \tag{2.9}$$

Moreover, the reference energy E_{v}^{0}, which should show in all the diagonal terms of the matrices, is set to zero for a bulk semiconductor. The matrix elements contain the general expressions for a strained wurtzite semiconductor, according to the equation (2.10 ~ 2.16),

$$F = \Delta_1 + \Delta_2 + \lambda + \theta \tag{2.10}$$

$$G = \Delta_1 - \Delta_2 + \lambda + \theta \tag{2.11}$$

$$\lambda = \frac{\hbar^2}{2m_0}(\mathrm{A}_1 k_z^2 + \mathrm{A}_2 k_t^2) + D_1\varepsilon_{zz} + D_2\left(\varepsilon_{zz} + \varepsilon_{yy}\right) \tag{2.12}$$

$$\theta = \frac{\hbar^2}{2m_0}(\mathrm{A}_3 k_z^2 + \mathrm{A}_4 k_t^2) + D_3\varepsilon_{zz} + D_4\left(\varepsilon_{zz} + \varepsilon_{yy}\right) \tag{2.13}$$

$$K_t = \frac{\hbar^2}{2m_0}\mathrm{A}_5 k_t^2 \tag{2.14}$$

$$H_t = \frac{\hbar^2}{2m_0}A_6 k_t k_z \tag{2.15}$$

$$\Delta = \sqrt{2}\Delta_3 \tag{2.16}$$

where the k_t, which is the magnitude of the in-plane wave vector in the $k_x - k_y$ plane, is equal to $\sqrt{{k_x}^2 + {k_y}^2}$. Parameter Δ_1 is the crystal-filed split energy, and the Δ_2, Δ_3 account for the spin-orbit interaction. The A_i's are the effective mass parameters, and the D_i's are the deformation potentials. The relationships between A_i's and D_i's, respectively, are shown as follows:

$$A_1 - A_2 = -A_3 = 2A_4, \quad A_3 + 4A_5 = \sqrt{2}A_6, \quad \Delta_2 = \Delta_3 \tag{2.17}$$

$$D_1 - D_2 = -D_3 = 2D_4, \quad D_3 + 4D_5 = \sqrt{2}D_6 \tag{2.18}$$

So only five parameters, which are A_1, A_2, A_5, Δ_1 and Δ_2, and three deformation potentials are essential for getting the valence-band structures.

The strain tensor parameter is related to the lattice mismatch of the QW and barrier layers, as the equation (2.19~ 2.21)

$$\varepsilon_{xx} = \varepsilon_{yy} = \frac{a_0 - a}{a} \tag{2.19}$$

$$\varepsilon_{zz} = -\frac{2C_{13}}{C_{33}}\varepsilon_{xx} \tag{2.20}$$

$$\varepsilon_{xy} = \varepsilon_{yz} = \varepsilon_{zx} = 0 \tag{2.21}$$

where a_0 and a are the lattice constants of the substrate and the layer material, and C_{13} and C_{33} are the stiffness constants. The spontaneous P_{SP} and piezoelectric P_{PZ} polarization fields, which cause the electric field, also need to be considered into the calculation. The spontaneous polarization uses the linear interpolation [36], and the piezoelectric polarization can be expressed as follows [37]:

$$P_{PZ} = 2d_{31}\left(C_{11} + C_{12} - \frac{2C_{13}^2}{C_{33}}\right)\varepsilon_{xx} \tag{2.22}$$

where d_{31} and C’s are piezoelectric coefficient and elastic stiffness coefficients, respectively.

The existence of both built-in polarization fields could make the energy band bending. The electrostatic fields in each layer (jth) as a result of total polarization fields can be expressed as the equation (2.23) [36]

$$E_{j} = \left(\sum_k l_k P_k/\varepsilon_k - P_{j}\sum_k l_k/\varepsilon_k\right)/\varepsilon_{j}\sum_k l_k/\varepsilon_k \tag{2.23}$$

where P is the total macroscopic polarization, ε is the static dielectric constant, and l is the thickness of each layer (kth and jth), which correspond to the subscripts k and j. Moreover, the electric field expression should satisfy the periodic boundary conditions for ensuring zero average electric field in the layers [36].

$$\sum_k l_k E_k = 0$$

where k should consist of all layers of the structure, including the active regions and barrier regions.

By using the calculated envelope functions, the optical transition matrix element relating nth-state in the conduction band and mth-state in the valence band can be computed by the following relations [31]:

TE-polarization ($\hat{x}$ or $\hat{y}$ polarization)

$$|(M_x)_{nm}^{\sigma}(k_t)|^2 = \frac{|\langle S|p_x|X\rangle|^2}{4} \cdot \left\{\left\langle \phi_n \middle| g_m^{(1)} \right\rangle^2 + \left\langle \phi_n \middle| g_m^{(2)} \right\rangle^2\right\} \qquad \text{for } \sigma\text{=U}$$

$$|(M_x)_{nm}^{\sigma}(k_t)|^2 = \frac{|\langle S|p_x|X\rangle|^2}{4} \cdot \left\{\left\langle \phi_n \middle| g_m^{(4)} \right\rangle^2 + \left\langle \phi_n \middle| g_m^{(5)} \right\rangle^2\right\} \qquad \text{for } \sigma\text{=L}$$

TM-polarization ($\hat{z}$ polarization)

$$|(M_z)_{nm}^{\sigma}(k_t)|^2 = \frac{|\langle S|p_z|Z\rangle|^2}{4} \cdot \left\langle \phi_n \middle| g_m^{(3)} \right\rangle^2 \qquad \text{for } \sigma\text{=U}$$

$$|(M_z)_{nm}^{\sigma}(k_t)|^2 = \frac{|\langle S|p_z|Z\rangle|^2}{4} \cdot \left\langle \phi_n \middle| g_m^{(6)} \right\rangle^2 \qquad \text{for } \sigma\text{=U}$$

where ϕ_n and g_m are conduction and valence band confined states, respectively. The upper and lower Hamiltonian blocks are indicated by σ=U and σ=L, respectively.

Based on the Fermi's Golden rule, the spontaneous emission rate for TE $(e = x)$ or TM $(e = y)$ polarizations can be obtained by considering all interband transitions between nth conduction sub-bands and mth valence sub-bands as follows [31]:

$$g_{SP}^{e}(\hbar\omega) = \frac{2q^2\pi}{n_r c \varepsilon_0 m_0^2 \omega L_\omega} \sum_{\sigma=\mathrm{U,L}} \sum_{n,m} \int \frac{k_t dk_t}{2\pi} |(M_e)_{nm}^{\sigma}(k_t)|^2$$

$$\cdot \frac{f_n^c(k_t)\left(1 - f_{\sigma m}^{v}(k_t)\right)(\gamma/\pi)}{\left(E_{\sigma,nm}^{cv}(k_t) - \hbar\omega\right)^2 + \gamma^2}$$

The equation (2.24~2.25) expresses the relation between the optical gains for the TE (g^{TE}) and TE (g^{TM}) and the spontaneous emission rate.

$$g^{TE}(\hbar\omega) = g_{SP}^{x}(\hbar\omega)\left[1 - exp\left(\frac{\hbar\omega - \Delta F}{k_B T}\right)\right] \tag{2.24}$$

$$g^{TM}(\hbar\omega) = g_{SP}^{z}(\hbar\omega)\left[1 - exp\left(\frac{\hbar\omega - \Delta F}{k_B T}\right)\right] \tag{2.25}$$

The TM-polarized optical gain is negligible for our structure, based on the case [30,31], and the TE-polarized is dominant. For the calculation of the spontaneous emission rate, the total momentum matrix element is the average of two TE-polarization components and one TM-polarization component [30]:

$$\left|M_{sp}\right|^2 = \frac{1}{3}(2|M_x|^2 + |M_z|^2) \tag{2.26}$$

The total spontaneous emission rate per unit volume per unit energy interval $(s^{-1}cm^{-3}eV^{-1})$ can be written as follows [31]:

$$r^{spon}(E = \hbar\omega) = \frac{n_e^2\omega^2}{\pi^2\hbar c^2}\frac{2\left(2g_{sp}^x + g_{sp}^z\right)}{3} \tag{2.27}$$

By integrating the equation (2.27) over the entire frequency range, the total spontaneous emission rate per unit volume could be expressed as:

$$R_{sp} = \int_0^\infty r^{spon}(\hbar\omega)d(\hbar\omega) \tag{2.28}$$

The finite difference method is used to solve the Schrödinger equations [38], and the spatial interval for the finite difference method is 1 Å.

2.3 The Establishment of Simulation

In this simulation, the conduction and valence band offset ratio of AlGaN and AlInN alloys are equal to 0.63:0.37 [31,37], which means that $\Delta E_c{:}\ \Delta E_v = 63{:}\,37$. The lattice constants a(x) of $A_xB_{1-x}N$, like $Al_xGa_{1-x}N$ and $Al_xIn_{1-x}N$, are predicted to follow the composition-weighted between the compounds AN and BN (Vegard's law) [39]:

$$a_{ABN}(x) = x * a_{AN} + (1 - x) * a_{BN} \tag{2.29}$$

The bowing parameter should be used for describing a first approximation by a parabolic model because of the existence of compositional nonlinearities. In particular, the possible nonlinear dependence of the spontaneous polarization could be described as following [40]:

$$P(A_x B_{1-x} N) = x * P(AN) + (1-x) * P(BN) - b_{AB} * x * (1-x) \tag{2.30}$$

The bowing parameter of nonlinear spontaneous polarization for the AlInN alloys is equal to 0.07 C/m^2, and for the AlGaN alloys, the following equation (2.31) is for calculating the parameter [37,41].

$$P_{sp}(Al_x Ga_{1-x} N) = -0.025 * x^2 - 0.019 * x - 0.007 \tag{2.31}$$

The determined valence band offsets (VBOs) for InN/GaN and GaN/AlN are almost equal to 0.8 eV and 0.6 eV, individually [42]. Other parameters that were used in our simulation could be obtained from Table 2.1.

Table 2.1 Material parameters of GaN, AlN, and InN used in the simulation.

Parameters	GaN	AlN	InN
Lattice constant (Å)			
a	3.189	3.112	3.548
Energy Parameters			
Eg(eV) at 300K	3.54	6.28	0.6405
$\boldsymbol{\Delta_{cr}}$(eV)	0.019	-0.164	0.041
$\boldsymbol{\Delta_{so}}$(eV)	0.014	0.019	0.001
Conduction-band effective masses			
$\boldsymbol{m_{\parallel}}^*/\boldsymbol{m_0}$ at 300K	0.18	0.31	0.11
$\boldsymbol{m_{\perp}}^*/\boldsymbol{m_0}$ at 300K	0.2	0.32	0.11

Valence-band effective mass parameters			
$\boldsymbol{A_1}$	-7.24	-3.86	-9.24
$\boldsymbol{A_2}$	-0.51	-0.25	-0.6
$\boldsymbol{A_3}$	6.73	3.58	8.68
$\boldsymbol{A_4}$	-3.36	-1.32	-4.34
$\boldsymbol{A_5}$	-3.40	-1.47	-5.11
$\boldsymbol{A_6}$	-4.90	-1.64	-5.96
Elastic stiffness constants			
$\boldsymbol{C_{11}}$(GPa)	367	396	223
$\boldsymbol{C_{12}}$(GPa)	135	137	115
$\boldsymbol{C_{13}}$(GPa)	100	120	124
$\boldsymbol{C_{33}}$(GPa)	392	395	182
Strain effect on the conduction band			
$\boldsymbol{a_{cz}}(\boldsymbol{eV})$	-4.9	-3.4	-4.9
$\boldsymbol{a_{ct}}(\boldsymbol{eV})$	-11.3	-11.8	-11.3
Deformation Potentials (eV)			
$\boldsymbol{D_1}$(eV)	0.7	-2.9	0.7
$\boldsymbol{D_2}$(eV)	2.1	4.9	2.1
$\boldsymbol{D_3}$(eV)	1.4	9.4	1.4
$\boldsymbol{D_4}$(eV)	-0.7	4.0	-0.7

The $ZnSiN_2$ has the direct bandgap and indirect bandgap. Optical transmittance spectra were used in combination with direct XPS measurements to determine the silicon and germanium composition in the alloy, and its bandgap [28]. The result show that the bandgap of $ZnSi_{1-x}Ge_xN_2$ alloy varies linearly with composition from 3.2eV (x=l) to 4.46eV (x=0) [22,28]. The other parameters for the $ZnSiN_2$ and $ZnGeN_2$ that were used in our simulation could be obtained from Table.2.2 [43-45].

Table 2.2 Material parameters of $ZnSiN_2$ and $ZnGeN_2$ used in the simulation

Parameters	$ZnSiN_2$	ZnGeN2
Lattice constant (Å)		
a	3.09	3.19
Energy Parameters		
Eg(eV) at 300K	4.46	3.4
$\boldsymbol{\Delta_{cr}}$(eV)	0.09	0.0645
$\boldsymbol{\Delta_{so}}$(eV)	0	0
Conduction-band effective masses		
$\boldsymbol{m_{\parallel}}^*/\boldsymbol{m_0}$ at 300K	0.29	0.16
$\boldsymbol{m_{\perp}}^*/\boldsymbol{m_0}$ at 300K	0.3	0.22
Valence-band effective mass parameters		
$\boldsymbol{A_1}$	-4.71	-6.87
$\boldsymbol{A_2}$	-0.26	-0.51
$\boldsymbol{A_3}$	4.11	6.44

$\boldsymbol{A_4}$	-1.93	-2.19
$\boldsymbol{A_5}$	-0.32	2.30
$\boldsymbol{A_6}$	-3.76	1.95
Elastic stiffness constants		
$\boldsymbol{C_{11}}$(GPa)	367	396
$\boldsymbol{C_{12}}$(GPa)	135	137
$\boldsymbol{C_{13}}$(GPa)	117	103
$\boldsymbol{C_{33}}$(GPa)	463	401

2.4 Design Specifications

In this thesis, we investigated five QW designs – (i) a 1.8nm $Al_{0.64}Ga_{0.36}N$/0.3nm $ZnSi_{0.26}Ge_{0.74}N_2$/0.6nm $Al_{0.64}Ga_{0.36}N$ QW (QW-A), (ii) a 1.8nm $Al_{0.64}Ga_{0.36}N$/0.5nm $ZnSi_{0.26}Ge_{0.74}N_2$/0.6nm $Al_{0.64}Ga_{0.36}N$ QW (QW-B), (iii) a 1.8nm $Al_{0.64}Ga_{0.36}N$/0.7nm $ZnSi_{0.26}Ge_{0.74}N_2$/0.6nm $Al_{0.64}Ga_{0.36}N$ QW (QW-C), (iv) a 1.5nm $Al_{0.64}Ga_{0.36}N$/0.3nm $Al_{0.33}Ga_{0.67}N$/0.3 nm $ZnSi_{0.26}Ge_{0.74}N_2$/0.3nm $Al_{0.33}Ga_{0.67}N$/0.3nm $Al_{0.64}Ga_{0.36}N$ (QW-D), and (v) a 1.5nm $Al_{0.88}In_{0.12}N$/0.3nm $Al_{0.33}Ga_{0.67}N$/0.3 nm $ZnSi_{0.26}Ge_{0.74}N_2$/0.3nm $Al_{0.33}Ga_{0.67}N$/0.3nm $Al_{0.88}In_{0.12}N$ (QW-E). The energy band alignments, electron-hole wavefunction overlaps, spontaneous emission spectra, spontaneous emission radiative recombination rates and material gain were calculated for each case. These results were compared with those of a conventional AlN/3nm $Al_{0.48}Ga_{0.52}N$/AlN QW (QW-F). Figure 2.3 illustrates the designs of QW-A through QW-F. The difference among QW-A, QW-B and QW-C is the thickness of the $ZnSi_{0.26}Ge_{0.74}N_2$ layers which are 0.3 nm, 0.5 nm and 0.7

nm, respectively. Moreover, the energy levels in the schematic keep going down with the increase of the thichness. In QW-D, a stepped Al compositions were used, which can be useful to address the lattice mismatch between the layers of III-N and Zn-IV-N_2 alloys. QW-E has a similar structure to QW-D except an $Al_{0.88}In_{0.12}N$ alloy was used in place of the $Al_{0.64}Ga_{0.36}N$ in the layer closest to the AlN barriers. In the novel QW structures (QW-A through QW-E), the $ZnSi_{0.26}Ge_{0.74}N_2$ works as the hole confinement layer due to its large valence band offset ($\Delta E_V = 0.8$ eV) with $Al_{0.64}Ga_{0.36}N$ [22-28].

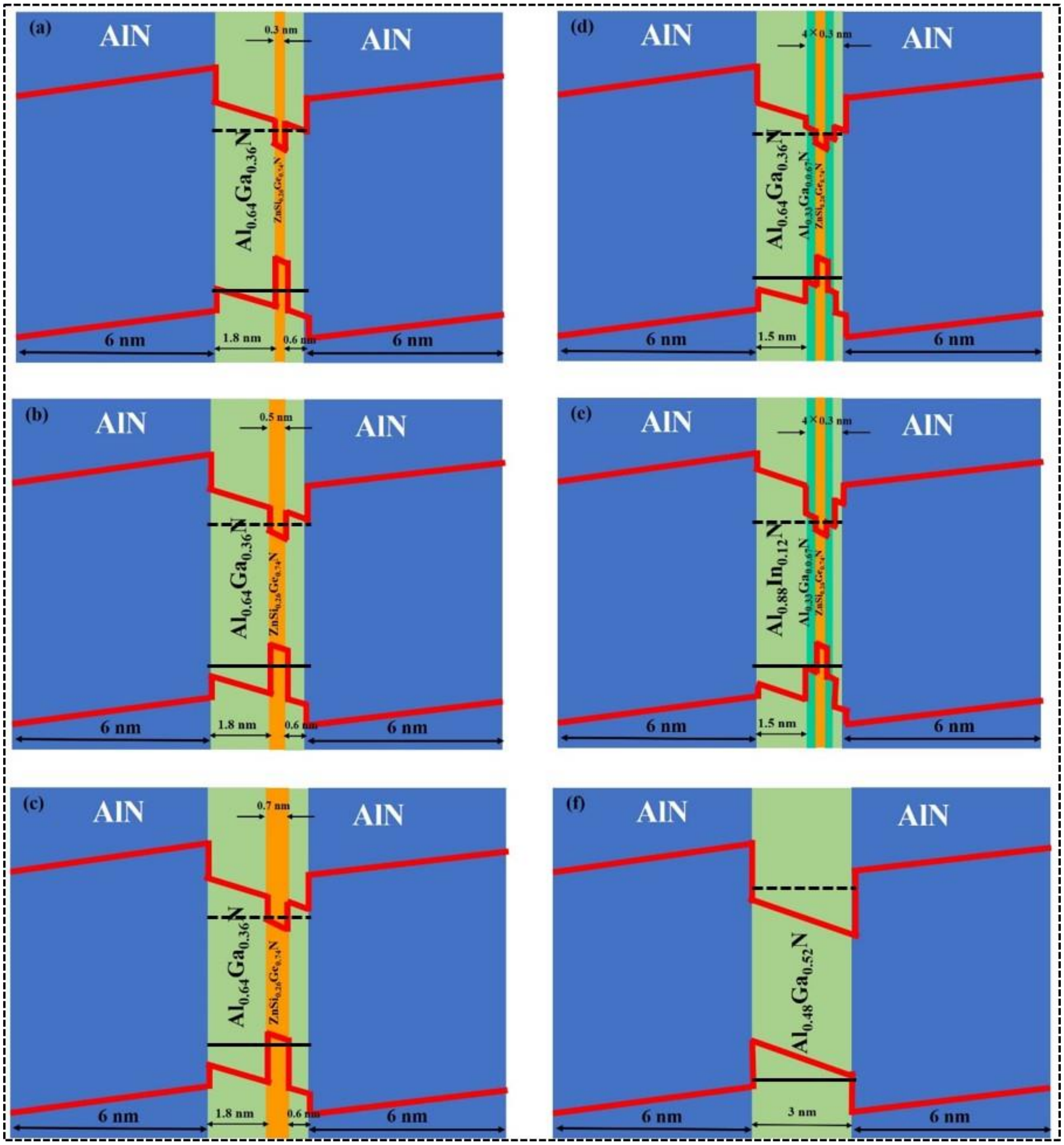

Figure 2.3 Schematic of the QW structure: (a) QW-A; (b) QW-B; (c) QW-C; (d) QW-D; (e) QW-E; (f) QW-F;

2.5 Band Structure Result

Figure 2.4 shows the band lineup and the electron−hole wave functions of the conventional 3 nm $Al_{0.48}Ga_{0.52}N$ QW (QW-F) at a carrier density of $n = 5\times10^{19}$ cm^{-3}. The peak spontaneous emission wavelength (λ_{peak}) of this structure was 270 nm. Because of the large polarization field in AlGaN, the conventional QW has significant charge separation resulting in an electron-hole wave function overlap ($\Gamma_{e\text{-}hh}$) of only 11%.

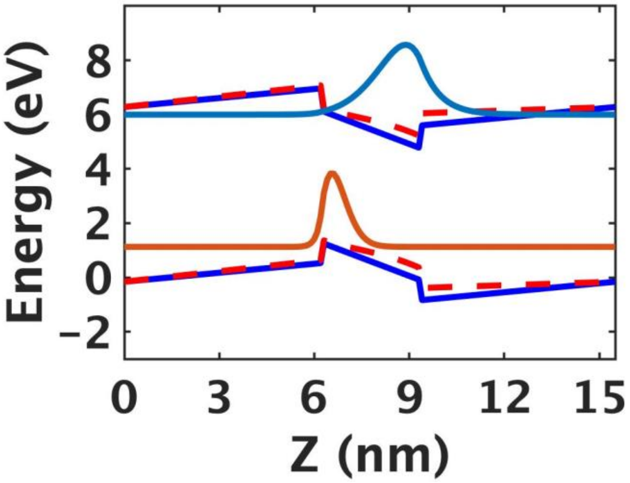

Figure 2.4 Band energy line-ups and electron and hole wavefunctions of the 3nm $Al_{0.48}Ga_{0.52}N$ QW. Blue line is the initial band lineup without self-consistent, and the red energy bands is with self-consistent.

The band alignment in the QW-A (AlN/1.8nm $Al_{0.64}Ga_{0.36}N$/0.3nm $ZnSi_{0.26}Ge_{0.74}N_2$/0.6nm $Al_{0.64}Ga_{0.36}N$/AlN), QW-B (AlN/1.8nm $Al_{0.64}Ga_{0.36}N$/0.5nm $ZnSi_{0.26}Ge_{0.74}N_2$/0.6nm $Al_{0.64}Ga_{0.36}N$/AlN) and QW-C (AlN/1.8nm $Al_{0.64}Ga_{0.36}N$/0.7nm $ZnSi_{0.26}Ge_{0.74}N_2$/0.6nm $Al_{0.64}Ga_{0.36}N$/AlN) are shown in Figures 2.5 (a-c), respectively. The peak emission wavelength increased with the increase in the thickness of the $ZnSi_{0.26}Ge_{0.74}N_2$ layer from

255 nm in QW-A to 271 nm in QW-B and 281 nm in QW-C. The electron-hole wavefunction overlap in QW-A, QW-B and QW-C were 46%, 51% and 51%, respectively. The remarkable enhancement of the electron-hole wavefunction overlap as compared to the conventional QW-F is attributed to the strong hole-confinement in the $ZnSi_{0.26}Ge_{0.74}N_2$ layer.

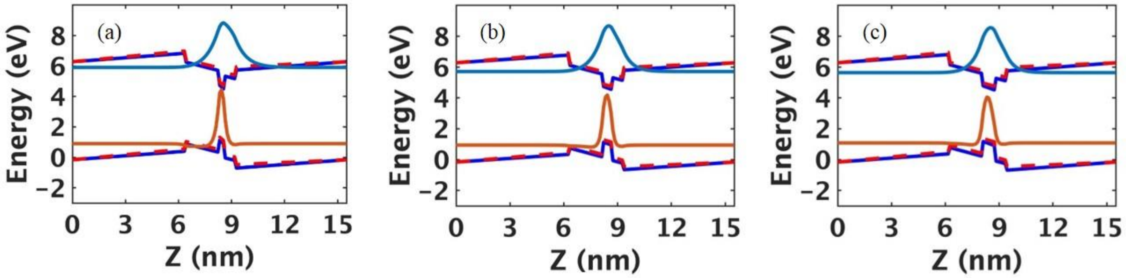

Figure 2.5 Band energy line-ups and electron-hole wavefunctions of the (a) QW-A, (b) QW-B and (c) QW-C

The lattice constant of $Al_{0.64}Ga_{0.36}N$ is equal to 3.1397 Å, and the lattice constant of $ZnSi_{0.26}Ge_{0.74}N_2$ is equal to 3.1640 Å which indicate a 0.8% lattice mismatch between these two alloys. The lattice mismatch between adjacent layers in heterostructure devices can result in a large density of defects in the active layer which in turn would be detrimental for radiative efficiency. The impacts of a large lattice mismatch between two adjacent layers can be avoided by using a graded alloy composition, as used in the design of QW-E and QW-F.

Figures 2.6 (b) and (d) show the band alignments in QW-D (AlN/1.5nm $Al_{0.64}Ga_{0.36}N$/0.3nm $Al_{0.33}Ga_{0.67}N$/0.3 nm $ZnSi_{0.26}Ge_{0.74}N_2$/0.3nm $Al_{0.33}Ga_{0.67}N$/0.3nm

$Al_{0.64}Ga_{0.36}N$ /AlN), and in QW-E (AlN/1.5nm $Al_{0.88}In_{0.12}N$/0.3nm $Al_{0.33}Ga_{0.67}N$/0.3 nm $ZnSi_{0.26}Ge_{0.74}N_2$/0.3nm $Al_{0.33}Ga_{0.67}N$/0.3nm $Al_{0.88}In_{0.12}N$ /AlN), respectively. The $Al_{0.64}Ga_{0.36}N/Al_{0.33}Ga_{0.67}N$ and $Al_{0.88}In_{0.12}N/Al_{0.33}Ga_{0.67}N$ configuration used in QW-D and QW-E between the AlN barrier and $ZnSi_{026}Ge_{0.74}N_2$ could effectively reduce the effects of lattice mismatch between the $Al_{0.64}Ga_{0.36}N$ and $ZnSi_{0.26}Ge_{0.74}N_2$. The position of the group-III nitride alloys and the Zn-IV-N_2 alloys used in these structures on the bandgap-vs-lattice constant plot are shown in Figures 2.6 (a) and (c), respectively. The calculated peak emission wavelength is ~270 nm for both QW-D and QW-E. The overlap between electron and hole wavefunctions were 48.5% and 51.5%, respectively.

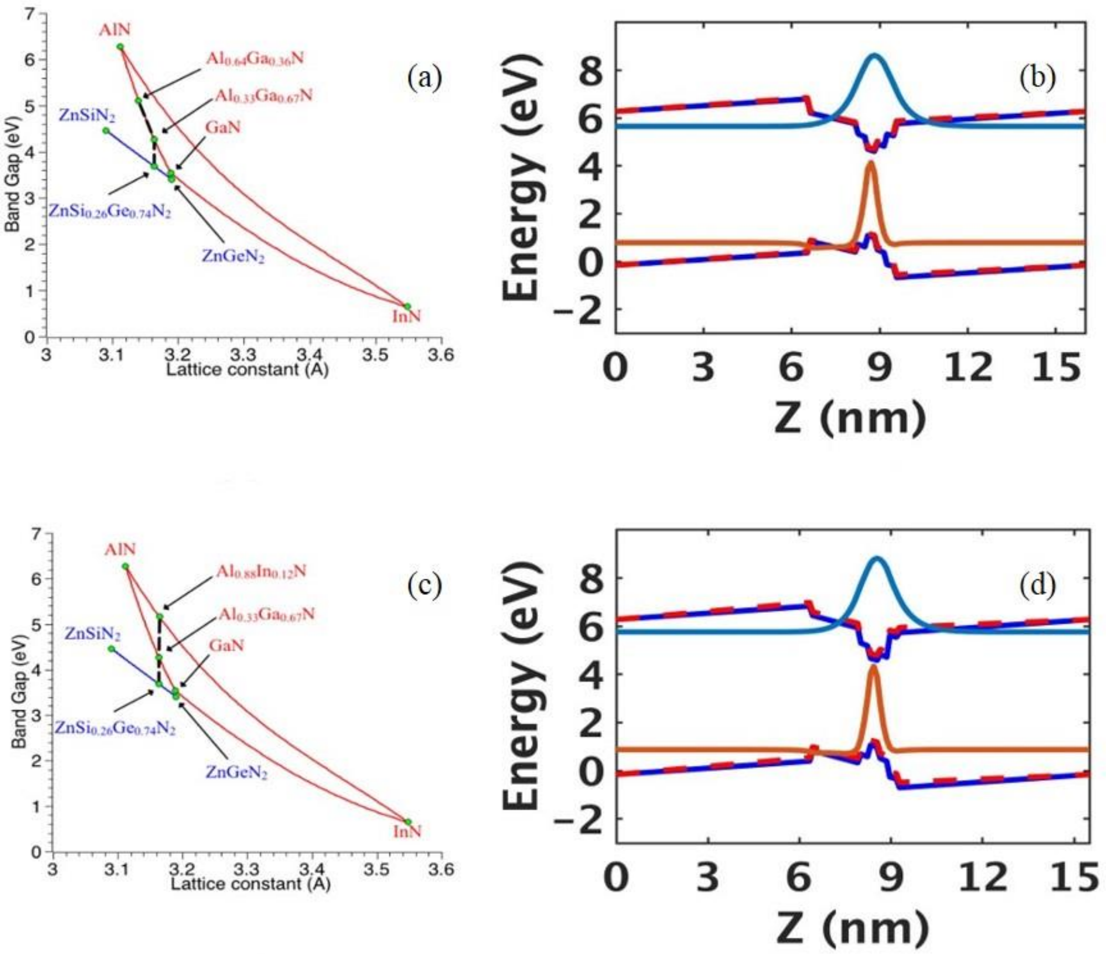

Figure 2.6 The lattice constant versus energy bandgap of (a) $Al_{0.64}Ga_{0.36}N$/ $Al_{0.33}Ga_{0.67}N$/ $ZnSi_{0.26}Ge_{0.74}N_2$ and (c) $Al_{0.88}In_{0.12}N$/ $Al_{0.33}Ga_{0.67}N$/ $ZnSi_{0.26}Ge_{0.74}N_2$, and energy-band line-ups versus electron-hole wavefunctions of (b) 1.5nm $Al_{0.64}Ga_{0.36}N$/0.3nm $Al_{0.33}Ga_{0.67}N$/0.3 nm $ZnSi_{0.26}Ge_{0.74}N_2$/0.3nm $Al_{0.33}Ga_{0.67}N$/0.3nm $Al_{0.64}Ga_{0.36}N$ and (d) 1.5nm $Al_{0.88}In_{0.12}N$/0.3nm $Al_{0.33}Ga_{0.67}N$/0.3 nm $ZnSi_{0.26}Ge_{0.74}N_2$/0.3nm $Al_{0.33}Ga_{0.67}N$/0.3nm $Al_{0.88}In_{0.12}N$. Blue line is the initial band lineup without self-consistent, and the red energy bands is with self-consistent.

2.4 Chapter Conclusion

In this chapter, we proposed the concept of AlInGaN/$ZnSiGeN_2$ QW structures with AlN barrier layers at the UV emitting wavelength range. The theoretical and numerical formulation of the 6-band $\boldsymbol{k} \cdot \boldsymbol{p}$ method was described. The simulation was performed using MATLAB (Mathworks [46]). The $ZnSiGeN_2$ layer works as the hole confinement layer, because of the large band offset. The results showed that the insertion of $ZnSiGeN_2$ layers in the QW could provide a notable enhancement in the hole carrier confinement. Moreover, the electron-hole wave function overlap for the novel QW design significantly increased 4~5 times from that of the 3 nm $Al_{0.48}Ga_{0.52}N$/AlN QW, which has a similar emitting wavelength. Furthermore, by adjusting the composition of each layer, the issue of the lattice mismatch could be resolved. The three layers of the novel $Al_{0.88}In_{0.12}N$/ $Al_{0.33}Ga_{0.67}N$/ $ZnSi_{0.26}Ge_{0.74}N_2$ QW have the same lattice constant, which means that this QW could fix severe defects of misfit dislocation.

Chapter 3. Spontaneous Emission Rate and Optical Gain Analysis

The energy band alignments presented in Chapter 2 indicate that a $ZnSiGeN_2$ layer inserted in AlN/AlGaN QWs can effectively confine the holes and thus, enhance the electron and hole wavefunction overlaps. Based on Fermi's golden rule, an enhancement in the electron-hole wavefunction overlap will enhance the spontaneous emission rate. In this chapter, we present the spontaneous emission radiative recombination rates for the conventional AlN/AlGaN/AlN QW (QW-F) as well for the novel AlN/AlInGaN/$ZnSiGeN_2$/AlInGaN/AlN QW structures (QW-A through QW-E). Numerical calculations indicated a 10X improvement in the spontaneous emission recombination rate for active layer carrier concentrations in the range of $n=1\text{-}5\times10^{18}$ cm^{-3} up to $n=1\text{-}5\times10^{19}$ cm^{-3}.

3.1 Spontaneous Emission Properties

The spontaneous emission spectra of the conventional as well as the novel QW structures were calculated by using the techniques described in Chapter 2. The spontaneous emission radiative recombination rates (R_{sp}) were calculated by integrating the spontaneous emission spectra over the entire wavelength range. In this section, we present the calculated spontaneous emission spectra and R_{sp} values for different QW structure discussed in Chapter 2.

3.1.1 The conventional QW

The spontaneous emission spectra of the AlN/3 nm $Al_{0.48}Ga_{0.52}N$/AlN conventional QW (QW-F) was calculated at a carrier density of n=1×10^{19} cm^{-3} to n=5×10^{19} cm^{-3}. As shown in Figure 3.1, the QW structure shows a peak emission wavelength of 271 nm, and the peak intensity of spontaneous emission is 8.6×10^{27} $s^{-1}cm^{-3}eV^{-1}$ at the carrier density of n=5×10^{19} cm^{-3}. With the decrease in the carrier concentration to 1×10^{19} cm^{-3}, the peak spontaneous emission intensity decreased to 0.5×10^{27} $s^{-1}cm^{-3}eV^{-1}$. Moreover, there was a redshift of the peak spontaneous emission wavelength of 271 nm with the decrease in carrier concentration from 5×10^{19} cm^{-3} to 1×10^{19} cm^{-3}, which is attributed to the carrier screening effect [47].

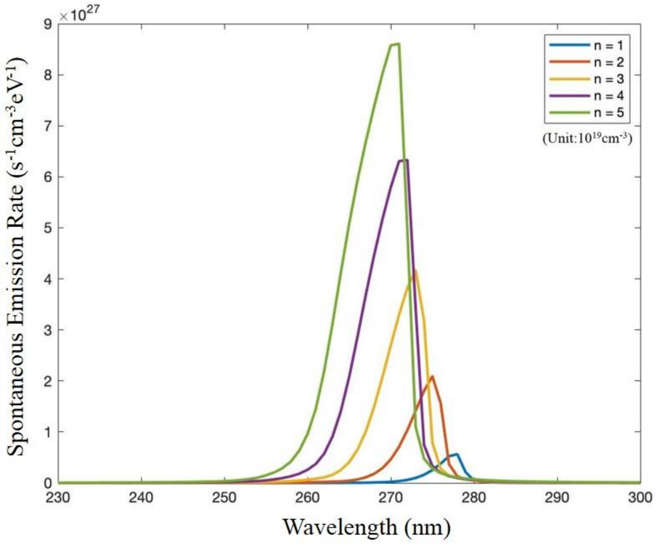

Figure 3.1 Spontaneous emission spectrum of conventional $Al_{0.48}Ga_{0.52}N$ QW at a carrier density of n=1×10^{19} cm^{-3} to n=5×10^{19} cm^{-3}

Figure 3.2 shows that the calculated R_{sp} values monotonically increases with the increase in the carrier concentrations, which is from 0.4×10^{28} $s^{-1}cm^{-3}$ to 7.2×10^{28} $s^{-1}cm^{-3}$ for the conventional QW for the carrier concentrations of n=1-5×10^{19} cm^{-3}.

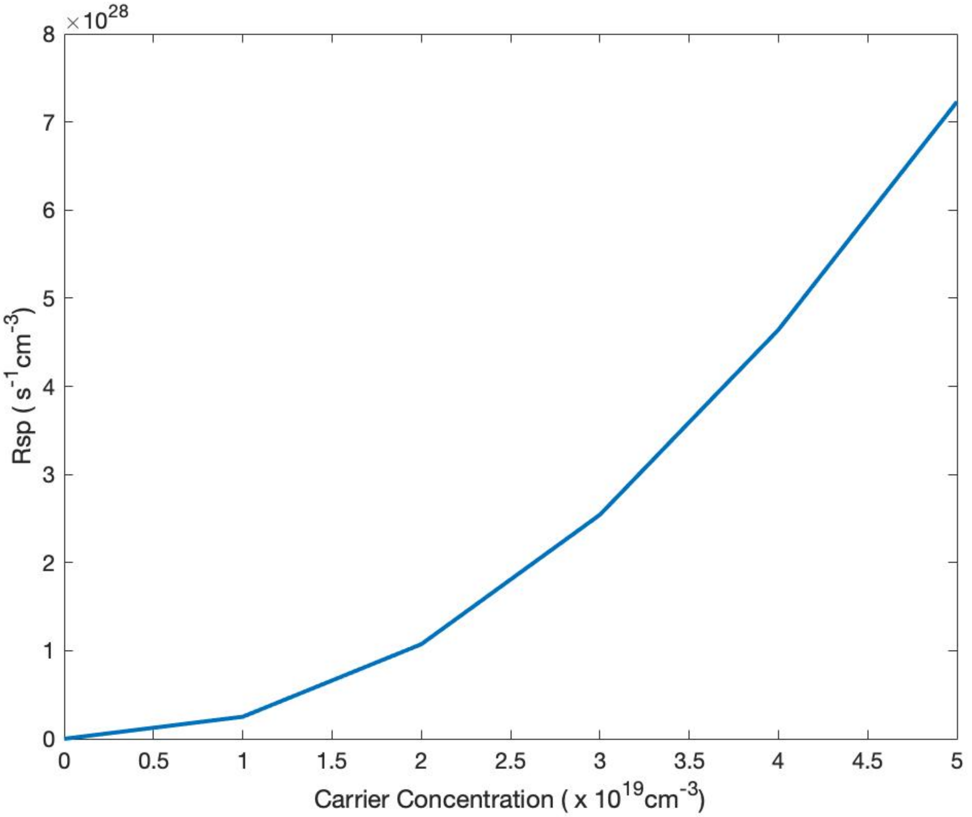

Figure 3.2 Spontaneous emission rate per unit volume (R_{sp}) of $Al_{0.48}Ga_{0.52}N$ QW

3.1.2 The $Al_{0.64}Ga_{0.36}N/ZnSi_{0.26}Ge_{0.74}N_2$ QW with the different thickness of $ZnSi_{0.26}Ge_{0.74}N_2$

Figure 3.3 plots the spontaneous emission spectra and spontaneous emission radiative rates for the AlN/2.4 nm $Al_{0.64}Ga_{0.36}N$/ 0.3 nm $ZnSi_{0.26}Ge_{0.74}N_2$/AlN QW (QW-A), AlN/2.4 nm $Al_{0.64}Ga_{0.36}N$/ 0.5 nm $ZnSi_{0.26}Ge_{0.74}N_2$/AlN QW (QW-B) and AlN/2.4 nm

$Al_{0.64}Ga_{0.36}N$/ 0.7 nm $ZnSi_{0.26}Ge_{0.74}N_2$/AlN QW (QW-C). The band alignments in these structures were shown in Figure 2.4. As can be seen from Figure 3.3, the peak intensity of the spontaneous emission rate increases from 0.8×10^{28} $s^{-1}cm^{-3}eV^{-1}$ to ~7.1×10^{28} $s^{-1}cm^{-3}eV^{-1}$ as the carrier concentration increases from $n=1\times10^{19}$ cm^{-3} to $n=5\times10^{19}$ cm^{-3} for all three structures. The peak spontaneous emission wavelength increased with the increase in the $ZnSi_{0.26}Ge_{0.74}N_2$ layer. The peak spontaneous emission wavelength of QW-A (0.3 nm thick $ZnSi_{0.26}Ge_{0.74}N_2$ layer) was 255 nm, which increased to 271 nm and 288 nm with the increase in the $ZnSi_{0.26}Ge_{0.74}N_2$ layer thickness to 0.5 nm and 0.7 nm, respectively. The redshift in the peak spontaneous emission wavelength due to carrier screening were 6-8 nm for $ZnSi_{0.26}Ge_{0.74}N_2$ layer thickness of 0.3 nm, 0.5 nm and 0.7 nm, respectively. Both the full width at half maximum of the spontaneous emission spectra and spontaneous emission radiative recombination rate increased slightly with increase in the $ZnSi_{0.26}Ge_{0.74}N_2$ layer thickness. The spontaneous emission radiative recombination rate values were 4.6×10^{29} $s^{-1}cm^{-3}$, 6.2×10^{29} $s^{-1}cm^{-3}$ and 6.9×10^{29} $s^{-1}cm^{-3}$ for 0.3 nm, 0.5 nm and 0.7 nm thickness of the $ZnSi_{0.26}Ge_{0.74}N_2$ layer a carrier density of $n=5\times10^{19}$ cm^{-3}.

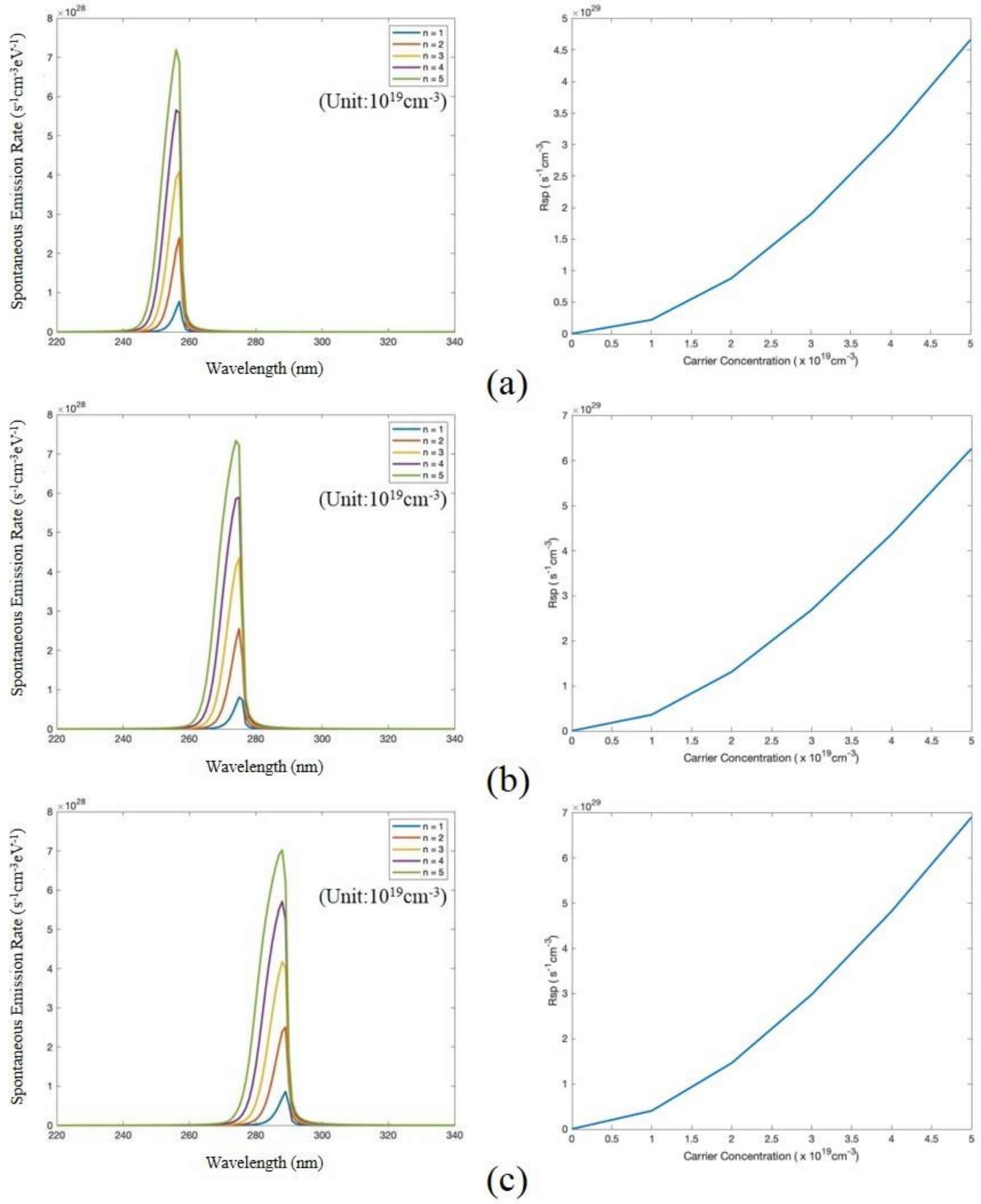

Figure 3.3 Spontaneous emission spectrum and spontaneous emission rate per unit volume (R_{sp}) of the $Al_{0.64}Ga_{0.36}N/ZnSi_{0.26}Ge_{0.74}N_2$ QW with (a) 0.3nm $ZnSi_{0.26}Ge_{0.74}N_2$ (b) 0.5nm $ZnSi_{0.26}Ge_{0.74}N_2$ and (c) 0.7nm $ZnSi_{0.26}Ge_{0.74}N_2$ for carrier concentration in the range of 1-5 $\times 10^{19}$ cm^{-3}

For low carrier concentration ($n<1\times10^{19}$ cm^{-3}) in LED devices, the carrier screening effect is less prominent, and the typical carrier concentration for LED operation ranges from n=2-5×10^{18} cm^{-3}. As can be seen from Figure 3.4 (a), the QW exhibited 9-11 times enhancement of spontaneous emission radiative recombination rate for low carrier concentration range of n=1×10^{18} cm^{-3} up to n=5×10^{18} cm^{-3}. Thus, the significant enhancement for the novel QW will lead to a significant improvement in the radiative efficiency of the LEDs. Moreover, Figure 3.4 (b) indicated a 10X improvement in peak spontaneous emission intensity by novel QW-A, QW-B and QW-C as compared to the conventional AlN/AlGaN/AlN QW-F in high carrier concentration range of 1-5 ×10^{19} cm^{-3} for laser operation. The R_{sp} keeps rising with the increase of the $ZnSi_{0.26}Ge_{0.74}N_2$ layer.

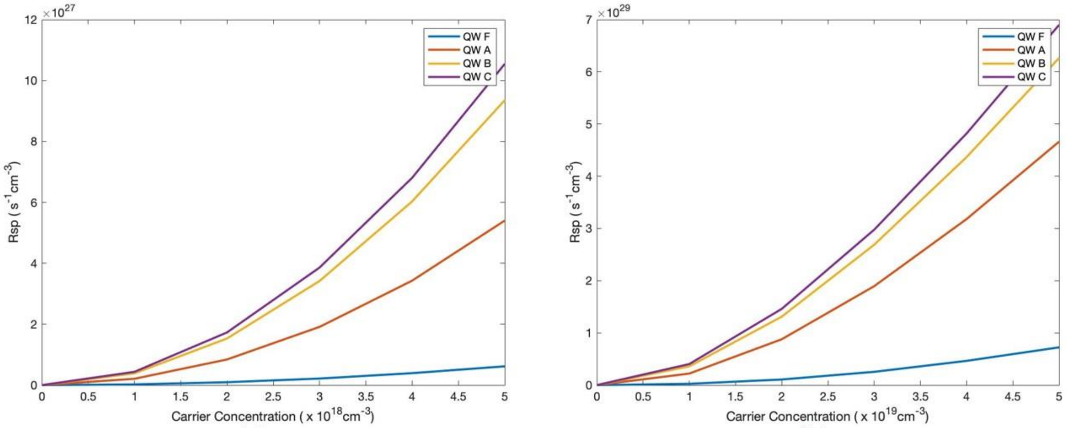

(a) (b)

Figure 3.4 The contrast of spontaneous emission rate per unit volume (R_{sp}) of QW-A, QW-B, QW-C and QW-F for carrier concentration in the range of (a) 1-5 ×10^{18} cm^{-3} (b) 1-5 ×10^{19} cm^{-3}

3.1.3 The step-like and Al-content graded QW

The lattice mismatch between the adjacent layers increases the density of defects in heterostructure devices or in other words, the density of non-radiative recombination has centers, which would have adverse impacts on the LED efficiency. One effective approach to address the lattice mismatch between the AlGaN and $ZnSiGeN_2$ layers can be the use of stepped Al-composition. The band alignments in two such device structures have been shown in Chapter 2 (Figure.). Figure 3.5 shows spontaneous emission spectra and spontaneous emission radiative recombination rate (R_{sp}) for QW-D (AlN/1.5 nm $Al_{0.64}Ga_{0.36}N$/0.3 nm $Al_{0.33}Ga_{0.67}N$/0.3 nm $ZnSi_{0.26}Ge_{0.74}N_2$/0.3 nm $Al_{0.33}Ga_{0.67}N$/0.3 nm $Al_{0.64}Ga_{0.36}N$/AlN) and QW-E (AlN/1.5nm $Al_{0.88}In_{0.12}N$/0.3nm $Al_{0.33}Ga_{0.67}N$/0.3 nm $ZnSi_{0.26}Ge_{0.74}N_2$/0.3nm $Al_{0.33}Ga_{0.67}N$/0.3nm $Al_{0.88}In_{0.12}N$/AlN). For QW-D, the Figure 3.5 shows that the peak intensity of spontaneous emission increases from 0.8×10^{28} $s^{-1}cm^{-3}eV^{-1}$ to 6.7×10^{28} $s^{-1}cm^{-3}eV^{-1}$ as the carrier concentration increases from $n=1\times10^{19}$ cm^{-3} to $n=5\times10^{19}$ cm^{-3}. For QW-E, the peak intensity of spontaneous emission increases from 0.5×10^{28} $s^{-1}cm^{-3}eV^{-1}$ to 4.8×10^{28} $s^{-1}cm^{-3}eV^{-1}$ for $n=1\sim5\times10^{19}$ cm^{-3}.

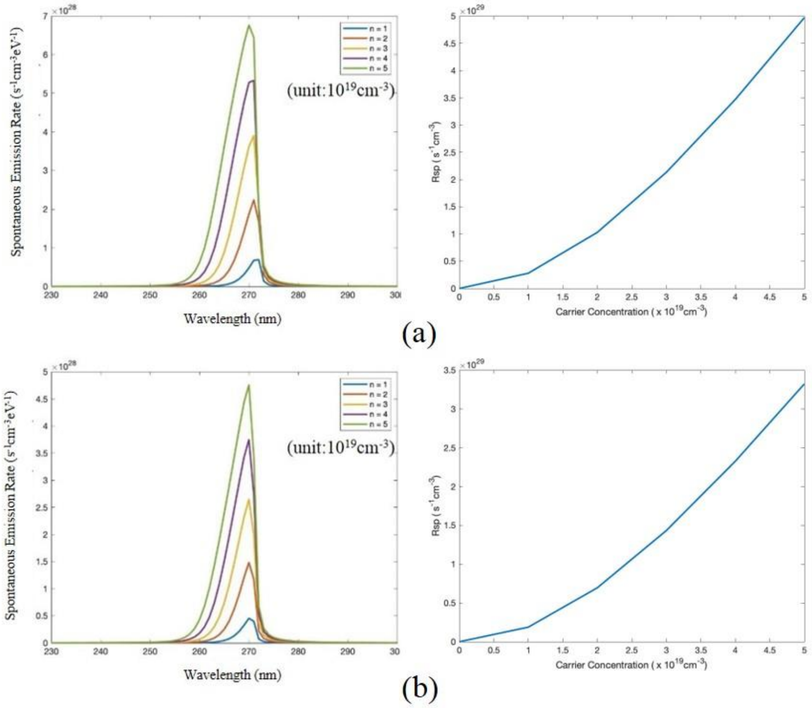

(a)

(b)

Figure 3.5 Spontaneous emission spectrum and spontaneous emission rate per unit volume (R_{sp}) of (a) 1.5nm $Al_{0.64}Ga_{0.36}N$/0.3nm $Al_{0.33}Ga_{0.67}N$/0.3 nm $ZnSi_{0.26}Ge_{0.74}N_2$/0.3nm $Al_{0.33}Ga_{0.67}N$/0.3nm $Al_{0.64}Ga_{0.36}N$ QW and (b) 1.5nm $Al_{0.88}In_{0.12}N$/0.3nm $Al_{0.33}Ga_{0.67}N$/0.3 nm $ZnSi_{0.26}Ge_{0.74}N_2$/0.3nm $Al_{0.33}Ga_{0.67}N$/0.3nm $Al_{0.88}In_{0.12}N$ QW for n=1~5×10^{19} cm^{-3}

For low carrier concentration case of n=5×10^{18} cm^{-3} in Figure 3.6 (a), the spontaneous emission radiative recombination rate of the step-like and Al-content graded QWs exhibits approximately a 8-9X improvement in contrast to that of the conventional QW. For high carrier concentration in the range of n=1-5×10^{19} cm^{-3}, the peak spontaneous emission radiative recombination rate values of in QW-D and QW-E were in the range of 3.3×10^{29} $s^{-1}cm^{-3}$ to 4.9×10^{29} $s^{-1}cm^{-3}$, which are slightly smaller as compared to QW-A through QW-

C presented in the previous section, and they still have almost 8 times enhancement in contrast to R_{sp} of the QW-F, as shown in Figure 3.6 (b).

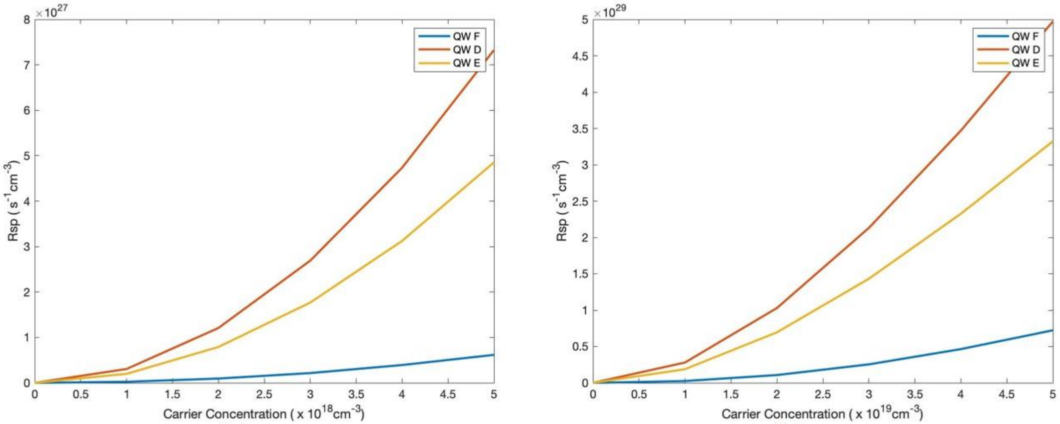

(a) (b)

Figure 3.6 The contrast of spontaneous emission rate per unit volume (R_{sp}) of QW-D, QW-E and QW-F for carrier concentration in the range of (a) 1-5 ×10^{18} cm^{-3} (b) 1-5 ×10^{19} cm^{-3}

3.2 Material Gain Properties

The TE-Polarized optical gain spectrum was calculated for both conventional and strain-compensate structures at a high carrier density ($n=5*10^{19}$ cm^{-3}).

3.2.1 The conventional QW

Figure 3.7 shows the TE-polarized material gain for the conventional QW-F (AlN/3 nm $Al_{0.64}Ga_{0.36}N$/AlN) is equal to 370.5 cm^{-1} at a carrier density of $n=5\times10^{19}$ cm^{-3}, and the emitting wavelength is at 270.9 nm.

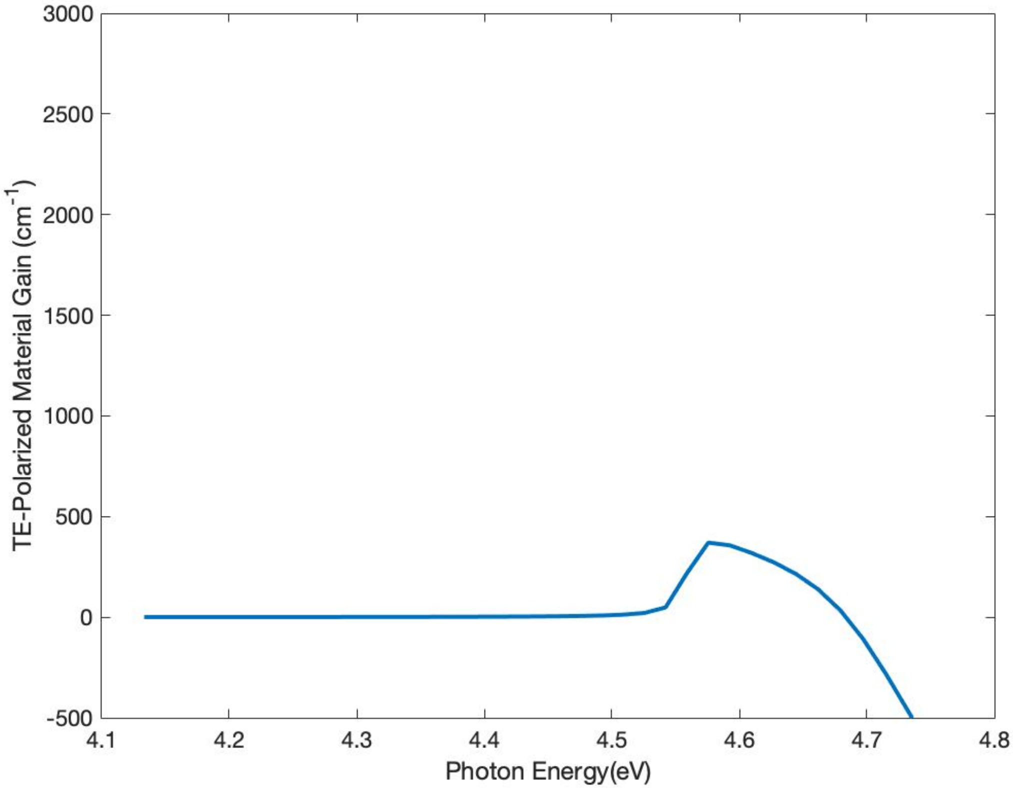

Figure 3.7 Optical gain spectrum of conventional $Al_{0.48}Ga_{0.52}N$ QW

3.2.2 The $Al_{0.64}Ga_{0.36}N/ZnSi_{0.26}Ge_{0.74}N_2$ QW with the different thickness of $ZnSi_{0.26}Ge_{0.74}N_2$

Optical gain spectra of QW-A, QW-B and QW-C are shown in Figures 3.8 (a-c), respectively. The peak TE-polarized material gain and corresponding wavelengths increased with the increase in the $ZnSi_{0.26}Ge_{0.74}N_2$ layer thickness. As can be seen from Figure 3.8, for $n = 5\times 10^{19}$ cm^{-3} carrier concentration, the peak TE-polarized material gains and corresponding wavelengths were 3352 cm^{-1} and 255 nm, 3997 cm^{-1} and 271 nm, and 4279 cm^{-1} and 288 nm for QW-A, QW-B and QW-C, respectively. Almost 10X improvement in the peak TE-polarized material gain in the novel QW-A through QW-C as compared to the conventional QW-F is attributed to the enhanced electron-hole wavefunction overlap provided by the $ZnSi_{0.26}Ge_{0.74}N_2$ layer, which resulted in larger transition matrix elements [30,31,48]. This lattice mismatch is a problem for growth, such as the formation of misfit dislocations throughout the film. As we discussed in the previous chapter, the Al-content is changed in the different layers.

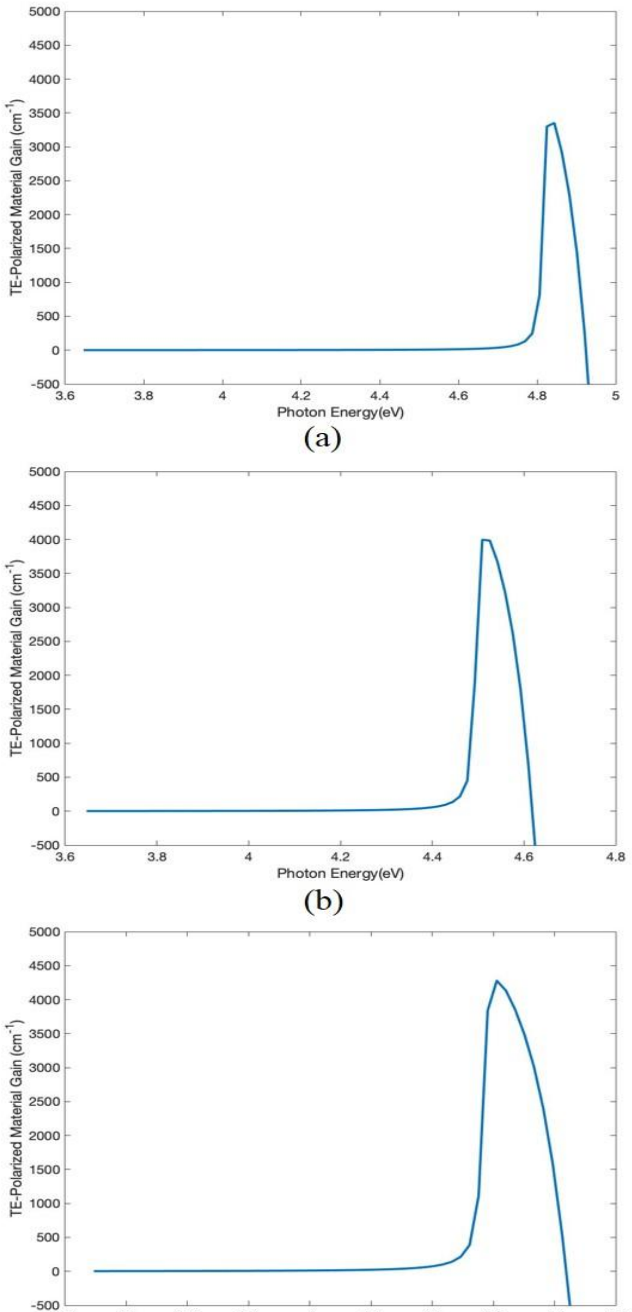

Figure 3.8 Optical gain spectrum of the $Al_{0.64}Ga_{0.36}N/ZnSi_{0.26}Ge_{0.74}N_2$ QW with (a) 0.3nm $ZnSi_{0.26}Ge_{0.74}N_2$, (b) 0.5nm $ZnSi_{0.26}Ge_{0.74}N_2$ and (c) 0.7nm $ZnSi_{0.26}Ge_{0.74}N_2$

3.2.3 The step-like and Al-content graded QW

The optical gain spectra of the strain-compensated novel QW structures, namely, QW-D (AlN/1.5 nm $Al_{0.64}Ga_{0.36}N$/0.3 nm $Al_{0.33}Ga_{0.67}N$/0.3 nm $ZnSi_{0.26}Ge_{0.74}N_2$/0.3 nm $Al_{0.33}Ga_{0.67}N$/0.3 nm $Al_{0.64}Ga_{0.36}N$/AlN) and QW-E (AlN/1.5nm $Al_{0.88}In_{0.12}N$/0.3nm $Al_{0.33}Ga_{0.67}N$/0.3 nm $ZnSi_{0.26}Ge_{0.74}N_2$/0.3nm $Al_{0.33}Ga_{0.67}N$/0.3nm $Al_{0.88}In_{0.12}N$/AlN), are shown in Figures 3.9 (a) and (b), respectively. For $n = 5\times 10^{19}$ cm^{-3} carrier concentration, the peak TE-polarized material gains and corresponding wavelengths were 3518 cm^{-1} and 20 nm, and 2500 cm^{-1} and 270 nm for QW-D and QW-E, respectively. These material gain values are smaller than those obtained for QW-A through QW-C. However, the QW-D and QW-E designs will potentially enjoy the benefits of reduced defect densities due to the reduced lattice mismatch.

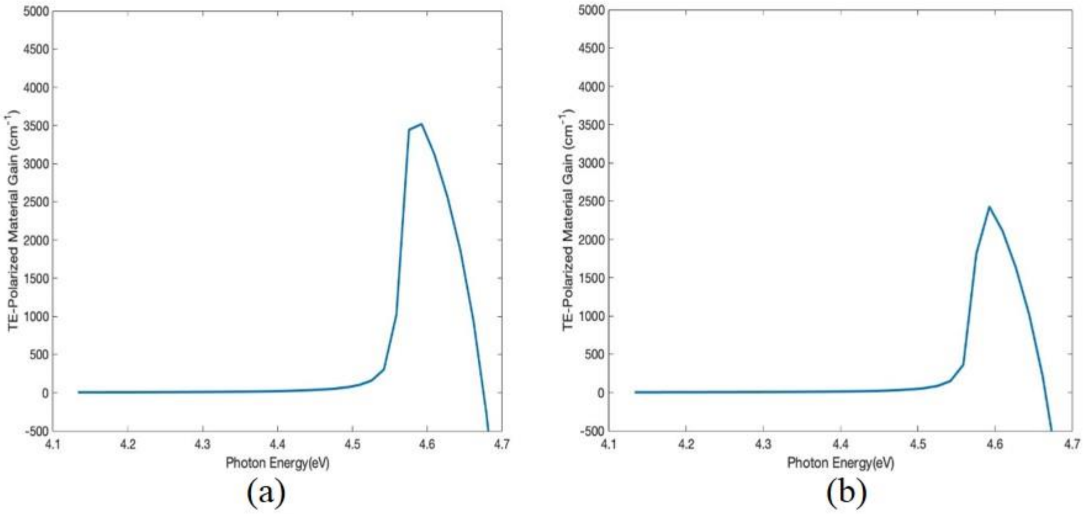

(a)

(b)

Figure 3.9 Optical gain spectra of (a) QW-D (AlN/1.5nm $Al_{0.64}Ga_{0.36}N$/0.3nm $Al_{0.33}Ga_{0.67}N$/0.3 nm $ZnSi_{0.26}Ge_{0.74}N_2$/0.3nm $Al_{0.33}Ga_{0.67}N$/0.3nm $Al_{0.64}Ga_{0.36}N$/AlN) and

(b) QW-E (AlN/1.5nm $Al_{0.88}In_{0.12}N$/0.3nm $Al_{0.33}Ga_{0.67}N$/0.3 nm $ZnSi_{0.26}Ge_{0.74}N_2$/0.3nm $Al_{0.33}Ga_{0.67}N$/0.3nm $Al_{0.88}In_{0.12}N$/AlN).

3.3 Summary

This chapter investigated the spontaneous emission rate of the conventional AlGaN/AlN QW and the novel $Al_{0.64}Ga_{0.36}N/ZnSi_{0.26}Ge_{0.74}N_2$/AlN QWs with the different thickness of II-IV-N_2 layer and the step-like and Al-content graded QW for decreasing the lattice mismatch. The use of the $ZnSiGeN_2$ layer could deal with the issue of the lattice mismatch and provide a significant enhancement, which is equal to almost 10 times in the spontaneous emission rate from low carrier concentration (n=1-5×10^{18} cm^{-3}) up to high carrier concentration (n=1-5×10^{19} cm^{-3}). The peak emission wavelength showed significant redshift with the increase in the $ZnSiGeN_2$ layer. The novel structure provides enhanced spontaneous emission rate, as compared to the conventional AlGaN/AlN design, even when an AlGaN layer with different Al composition or the AlGaN layer is replaced by an AlInN layer, although the magnitude of the enhancement might decrease. To address the lattice mismatch between adjacent layers in the novel design a graded Al composition AlGaN layer can be used, which was also found to provide improved spontaneous emission rate. In addition, the enhanced material gain of the novel QW structure as compared to the conventional design at a relatively high carrier concentration of 5×10^{19} cm^{-3} indicates that these structures can potentially be used in UV laser diodes. Therefore, the novel AlInGaN/$ZnSiGeN_2$ heterostructure QW investigated in this thesis can potentially be used for high-efficiency UV emitters.

Chapter 4. Conclusion and Future Work

4.1 Summary

In this thesis, a new type of quantum well (QW) structure based on AlInGaN/ZnSiGeN$_2$ was successfully demonstrated. This thesis presents self-consistent comprehensive theoretical and numerical studies on the electron-hole wave function overlap, spontaneous emission, and optical gain properties. Due to the existence of the ZnSiGeN$_2$ as the hole confinement layer, the lattice mismatch is decreased, and the material quality could be improved. The simulation of the energy dispersion is based on a 6-band $\boldsymbol{k} \cdot \boldsymbol{p}$ formalism, and this method contains the valence band mixing, strain effect, spontaneous and piezoelectric polarization, and carrier screening. The main research results are summarized as follows:

1. The band lineups of a conventional AlGaN QW and AlInGaN/ZnSiGeN$_2$ based QW were calculated using a 6 band *k.p* method. The ZnSiGeN$_2$ layer works as the hole confinement layer due to the large valence band between used AlGaN and ZnSiGeN$_2$ compositions. The effects of the thickness of the ZnSiGeN$_2$ layer were investigated. In addition, two strain-compensated designs with stepped Al-composition alloys were also investigated. The electron-hole wavefunction overlap increased by almost 4.5X in the novel designs (close to 50%) as compared to the conventional structure (11%).

2. From our simulation, both the spontaneous emission spectra and optical gain of the AlInGaN/ZnSiGeN$_2$ QW demonstrate enhancement compared with those of the conventional QW.

4.2 Future Work

Based on the current research and studies in the simulation for designing UV light-emitting diodes (LEDs), there are several opportunities and directions for future work.

1. Understanding the comprehensive theoretical model, which is based on the effective-mass Hamiltonian by using the 6-band $\boldsymbol{k} \cdot \boldsymbol{p}$ method for calculating the electronic band structures and optical gain, to a deep level.
2. UV-LEDs are the most important for environmentally friendly methods of producing UV light. UV LEDs have seen tremendous growth over the past several years. The simulation of UV-LEDs should be continuously studied by using the newly synthesized material.
3. Based on the calculation of the material gain, more researches could focus on the impact of this QW on real devices of laser structures.
4. The development and synthesis of this kind of AlInGaN/ZnSiGeN$_2$ QW should be deeply studied by using some advanced growth methods, for instance, MOCVD or other simple growth methods.

Bibliography

[1]. M. Pattison, 2018 Solid-State Lighting R&D Opportunities. 2019.

[2]. H. KITABAYASHI, Y. KAWABATA, H. MATSUBARA, K.-ichi MIYAHARA, and S. TANAKA, "Development of High Power Infrared LED," *ELECTRONICS*, pp. 71–74, Apr. 2010.

[3]. M. A. Khan, "AlGaN multiple quantum well based deep UV LEDs and their applications," *phys. stat. sol. (a)*, vol. 203, no. 7, pp. 1764–1770, May 2006.

[4]. H. Hirayama, "Recent Progress in AlGaN Deep-UV LEDs," *Light-Emitting Diode - An Outlook On the Empirical Features and Its Recent Technological Advancements*, 2018.

[5]. A. Zyara, H. Heinonen-Tanski, A.-M. Veijalainen, and E. Torvinen, "UV-LEDs Efficiently Inactivate DNA and RNA Coliphages," *Water*, vol. 9, no. 1, p. 46, Dec. 2017.

[6]. E. A. Jones, F. F. Wang, and D. Costinett, "Review of Commercial GaN Power Devices and GaN-Based Converter Design Challenges," *IEEE Trans. Emerg. Sel. Topics Power Electron.*, vol. 4, no. 3, pp. 707–719, Sep. 2016.

[7]. H. Hirayama, "Quaternary InAlGaN-based high-efficiency ultraviolet light-emitting diodes," *J. Appl. Phys.*, vol. 97, no. 9, p. 091101, 2005.

[8]. J. Han, M. H. Crawford, R. J. Shul, J. J. Figiel, M. Banas, L. Zhang, Y. K. Song, H. Zhou, and A. V. Nurmikko, "AlGaN/GaN quantum well ultraviolet light emitting diodes," *Appl. Phys. Lett.*, vol. 73, no. 12, pp. 1688–1690, 1998.

[9]. A. Kinoshita, H. Hirayama, M. Ainoya, Y. Aoyagi, and A. Hirata, “Room-temperature operation at 333 nm of $Al_{0.03}Ga_{0.97}N/Al_{0.25}Ga_{0.75}N$ quantum-well light-emitting diodes with Mg-doped superlattice layers,” *Appl. Phys. Lett.*, vol. 77, no. 2, pp. 175–177, Oct. 2000.

[10]. W. Sun, V. Adivarahan, M. Shatalov, Y. Lee, S. Wu, J. Yang, J. Zhang, and M. A. Khan, “Continuous Wave Milliwatt Power AlGaN Light Emitting Diodes at 280 nm,” *Jpn. J. Appl. Phys.*, vol. 43, no. No. 11A, Aug. 2004.

[11]. V. Adivarahan, S. Wu, J. P. Zhang, A. Chitnis, M. Shatalov, V. Mandavilli, R. Gaska, and M. A. Khan, “High-efficiency 269 nm emission deep ultraviolet light-emitting diodes,” *Appl. Phys. Lett.*, vol. 84, no. 23, pp. 4762–4764, Jul. 2004.

[12]. V. Adivarahan, W. H. Sun, A. Chitnis, M. Shatalov, S. Wu, H. P. Maruska, and M. A. Khan, “250nmAlGaN light-emitting diodes,” *Appl. Phys. Lett.*, vol. 85, no. 12, pp. 2175–2177, 2004.

[13]. M. Shatalov, W. Sun, A. Lunev, X. Hu, A. Dobrinsky, Y. Bilenko, J. Yang, M. Shur, R. Gaska, C. Moe, G. Garrett, and M. Wraback, “AlGaN Deep-Ultraviolet Light-Emitting Diodes with External Quantum Efficiency above 10%,” *Appl. Phys. Express*, vol. 5, no. 8, p. 082101, Nov. 2012.

[14]. H. Hirayama, T. Yatabe, N. Noguchi, T. Ohashi, and N. Kamata, “231–261nm AlGaN deep-ultraviolet light-emitting diodes fabricated on AlN multilayer buffers grown by ammonia pulse-flow method on sapphire,” *Appl. Phys. Lett.*, vol. 91, no. 7, p. 071901, 2007.

[15]. G. Liu, J. Zhang, X.-H. Li, G. Huang, T. Paskova, K. R. Evans, H. Zhao, and N. Tansu, "Metalorganic vapor phase epitaxy and characterizations of nearly-lattice-matched AlInN alloys on GaN/sapphire templates and free-standing GaN substrates," *J. Cryst. Growth*, vol. 340, no. 1, pp. 66–73, 2012.

[16]. C.-K. Tan, W. Sun, D. Borovac, and N. Tansu, "Large Optical Gain AlInN-Delta-GaN Quantum Well for Deep Ultraviolet Emitters," *Sci. Rep.*, vol. 6, no. 1, Oct. 2016.

[17]. A. Punya, T. R. Paudel, and W. R. L. Lambrecht, "Electronic and lattice dynamical properties of II-IV-N_2 semiconductors," *Phys. Status Solidi C,* vol. 8, no. 7-8, pp. 2492–2499, Jun. 2011.

[18]. P. Atchara and L. Walter R. L., "Band offsets between $ZnGeN_2$, GaN, ZnO, and $ZnSnN_2$ and their potential impact for solar cells," *Phys. Rev. B*, vol. 88, no. 7, pp. 075302–075308, Aug. 2013.

[19]. L. Han, K. Kash, and H. Zhao, "Designs of blue and green light-emitting diodes based on type-II InGaN-$ZnGeN_2$ quantum wells," *J. Appl. Phys.*, vol. 120, no. 10, p. 103102, Aug. 2016.

[20]. M. R. Karim, H. Ahmad, S. Ghosh, and B. M. A. Rahman, "Design of dispersion-engineered As_2Se_3 channel waveguide for mid-infrared region supercontinuum generation," *J. Appl. Phys.*, vol. 123, no. 21, p. 213101, Jul. 2018.

[21]. H. Fu, J. C. Goodrich, O. Ogidi-Ekoko, and N. Tansu, "Type-II AlInN/$ZnGeN_2$ quantum wells for ultraviolet laser diodes," *J. Appl. Phys.*, vol. 126, no. 13, p. 133103, Jul. 2019.

[22]. J. Muth, A. Cai, A. Osinsky, H. Everitt, B. Cook, and I. Avrutsky, “Optical Properties of II-IV-N_2 Semiconductors,” *MRS Proceedings*, vol. 831, 2004.

[23]. T. Cloitre, A. Sere, and R. Aulombard, “Epitaxial growth of $ZnSiN_2$ single-crystalline films on sapphire substrates,” *Superlattices and Microstructures*, vol. 36, no. 4-6, pp. 377–383, 2004.

[24]. B. P. Cook, H. O. Everitt, I. Avrutsky, A. Osinsky, A. Cai, and J. F. Muth, “Refractive indices of $ZnSiN_2$ on r-plane sapphire,” *Appl. Phys. Lett.*, vol. 86, no. 12, p. 121906, 2005.

[25]. L. Zhu, P. Norris, and L. Bouthillette, “Electronic Bandgap and Refractive Index Dispersion of Single Crystalline Epitaxial $ZnGeN_2$,” *MRS Proceedings*, vol. 607, 1999.

[26]. M. R. Karim, B. H. D. Jayatunga, Z. Feng, K. Kash, and H. Zhao, “Metal–Organic Chemical Vapor Deposition Growth of $ZnGeN_2$ Films on Sapphire,” *Cryst. Growth Des.*, vol. 19, no. 8, pp. 4661–4666, Mar. 2019.

[27]. T. Misaki, K. Tsuchiya, D. Sakai, A. Wakahara, H. Okada, and A. Yoshida, “Growth and Characterization of $ZnGeN_2$ by Using Remote-Plasma Enhanced Metalorganic Vapor Phase Epitaxy,” *Phys. Status Solidi C*, vol. 0, no. 1, pp. 188–191, 2003.

[28]. A. Osinsky, V. Fuflyigin, L. Zhu, A. Goulakov, J. Graff, and E. Schubert, “New concepts and preliminary results for SiC bipolar transistors: $ZnSiN_2$ and $ZnGeN_2$ heterojunction emitters,” *Proceedings 2000 IEEE/ Cornell Conference on High Performance Devices (Cat. No.00CH37122)*, pp. 168–172, Aug. 2002.

[29]. S. L. Chuang and C. S. Chang, “k·p method for strained wurtzite semiconductors,” *Phys. Rev. B*, vol. 54, no. 4, pp. 2491–2504, 1996.

[30]. S. L. Chuang, "Optical gain of strained wurtzite GaN quantum-well lasers," *IEEE J. Quantum Electron.*, vol. 32, no. 10, pp. 1791-1800, Oct. 1996.

[31]. H. Zhao, R. A. Arif, Y. Ee and N. Tansu, "Self-Consistent Analysis of Strain-Compensated InGaN–AlGaN Quantum Wells for Lasers and Light-Emitting Diodes," *IEEE J. Quantum Electron.*, vol. 45, no. 1, pp. 66-78, Jan. 2009.

[32]. C.-T. Kuo, K.-K. Chang, H.-W. Shiu, and C.-R. Liu, “Natural band alignments of InN/GaN/AlN nanorod heterojunctions,” *Appl. Phys. Lett.*, vol. 99, no. 12, p. 122101, 2011.

[33]. S. Lyu and W. R. L. Lambrecht, “Band alignment of III-N, ZnO and II–IV-N_2 semiconductors from the electron affinity rule,” *J. Phys. D*, vol. 53, no. 1, p. 015111, Jan. 2019.

[34]. A. P. Jaroenjittichai, S. Lyu, and W. R. L. Lambrecht, “Erratum: Band offsets between $ZnGeN_2$, GaN, ZnO, and $ZnSnN_2$ and their potential impact for solar cells [Phys. Rev. B 88, 075302 (2013)],” *Phys. Rev. B*, vol. 96, no. 7, p. 079907, Aug. 2017.

[35]. S. L. Chuang and C. S. Chang, “Effective - mass Hamiltonian for strained wurtzite GaN and analytical solutions,” *Appl. Phys. Lett.*, vol. 68, no. 12, pp. 1657–1659, 1996.

[36]. F. Bernardini and V. Fiorentini, “Spontaneous versus Piezoelectric Polarization in III-V Nitrides: Conceptual Aspects and Practical Consequences,” *Phys. Status Solidi B*, vol. 216, no. 1, pp. 391–398, Nov. 1999.

[37]. O. Ambacher, J. Majewski, C. Miskys, A. Link, M. Hermann, M. Eickhoff, M. Stutzmann, F. Bernardini, V. Fiorentini, V. Tilak, B. Schaff, and L. F. Eastman, “Pyroelectric properties of Al(In)GaN/GaN hetero- and quantum well structures,” *J. Phys. Condens. Matter*, vol. 14, no. 13, pp. 3399–3434, Apr. 2002.

[38]. S. L. Chuang and C. S. Chang, “A band-structure model of strained quantum-well wurtzite semiconductors,” *Semicond. Sci. Technol.*, vol. 12, no. 3, pp. 252–263, Mar. 1997.

[39]. A. Zoroddu, F. Bernardini, P. Ruggerone, and V. Fiorentini, “First-principles prediction of structure, energetics, formation enthalpy, elastic constants, polarization, and piezoelectric constants of AlN, GaN, and InN: Comparison of local and gradient-corrected density-functional theory,” *Phys. Rev. B*, vol. 64, no. 4, p. 045208, Jul. 2001.

[40]. F. Bernardini and V. Fiorentini, “Nonlinear macroscopic polarization in III-V nitride alloys,” *Phys. Rev. B*, vol. 64, no. 8, p. 085207, Aug. 2001.

[41]. J. Pal, G. Tse, V. Haxha, M. A. Migliorato, and S. Tomić, “Second-order piezoelectricity in wurtzite III-N semiconductors,” *Phys. Rev. B*, vol. 84, no. 8, p. 085211, Aug. 2011.

[42]. C.-T. Kuo, K.-K. Chang, H.-W. Shiu, and C.-R. Liu, “Natural band alignments of InN/GaN/AlN nanorod heterojunctions,” *Appl. Phys. Lett.*, vol. 99, no. 12, p. 122101, 2011.

[43]. P. Atchara and L. Walter R. L., “Band offsets between $ZnGeN_2$, GaN, ZnO, and $ZnSnN_2$ and their potential impact for solar cells,” *Phys. Rev. B*, vol. 88, no. 7, pp. 075302–075308, Aug. 2013.

[44]. S. Lyu and W. R. L. Lambrecht, “Band alignment of III-N, ZnO and II–IV-N_2 semiconductors from the electron affinity rule,” *J. Phys. D*, vol. 53, no. 1, p. 015111, Jan. 2019.

[45]. T. R. Paudel and W. R. L. Lambrecht, “First-principles calculations of elasticity, polarization-related properties, and nonlinear optical coefficients in Zn-IV-N2compounds,” *Phys. Rev. B*, vol. 79, no. 24, p. 245205, Jun. 2009.

[46]. “Makers of MATLAB and Simulink,” *MathWorks*. [Online]. Available: https://www.mathworks.com/. [Accessed: 17-Apr-2020].

[47]. S.-K. Zhang, W. Wang, R. R. Alfano, A. M. Dabiran, A. M. Wowchak, and P. P. Chow, “Carrier screening effect in AlGaN quantum-well avalanche photodiode,” *Gallium Nitride Materials and Devices IV*, Feb. 2009.

[48]. G. Lasher and F. Stern, “Spontaneous and Stimulated Recombination Radiation in Semiconductors,” *Phys. Rev.,* vol. 133, no. 2A, Jan. 1964.